

IMPROVING OPERATIONAL EFFICIENCY OF SMALL UNMANNED AIRCRAFT  
SYSTEMS FOR REMOTE SENSING APPLICATIONS

By

BRANDON SCOTT EVERS

A THESIS PRESENTED TO THE GRADUATE SCHOOL  
OF THE UNIVERSITY OF FLORIDA IN PARTIAL FULFILLMENT  
OF THE REQUIREMENTS FOR THE DEGREE OF  
MASTER OF SCIENCE

UNIVERSITY OF FLORIDA

2011

© 2011 Brandon Scott Evers

To Mom, Dad, Megan, and Heather

## ACKNOWLEDGMENTS

Thank you, Mom and Dad, for giving me the early tools to succeed and the patience and encouragement to pursue an advanced degree without the pressure to get a “real” job. Heather, thank you for always being there as a constant source of support and happiness. I can’t wait to see what our future together brings.

I owe a huge debt of gratitude to the interdisciplinary team of researchers contributing to the UF UASRG, whose passion and support have fostered a truly unique and successful program. Dr. Ifju, thank you for providing me with the amazing opportunity to work in such an exciting field and for your academic guidance throughout my college career. Dr. Percival, thank you for your years of work keeping this project moving and focused on quality science despite a constantly changing funding environment. Matt, your infinite patience and ability to juggle conflicting demands from all directions has kept us all working smoothly and I wish you luck as you begin your doctoral studies. Drs. Dewitt and Smith, I truly feel lucky to have worked with such a broad range of researchers from varying disciplines; the collaboration among sciences has created something great.

Finally, I thank my colleagues for their innumerable hours spent working on this project. John, thanks for all your work pushing the project towards operational success and for the confidence to press on with another generation of development. Thomas Rambo, thank you for your efforts in the field and for your huge contributions to the autopilot integration code. Thomas Reed, it’s been a pleasure to crank out airframes with you and your work as on-call machinist has been invaluable. I look forward to working with you all for some time to come.

## TABLE OF CONTENTS

	<u>page</u>
ACKNOWLEDGMENTS.....	4
LIST OF TABLES.....	7
LIST OF FIGURES.....	8
LIST OF ABBREVIATIONS.....	12
ABSTRACT.....	16
CHAPTER	
1 INTRODUCTION.....	18
Motivation.....	18
The UF Nova Project.....	19
Directly Georeferenced Aerial Photogrammetry.....	20
2 NOVA PROJECT PLATFORM DEVELOPMENT.....	24
Legacy Systems.....	24
Lessons Learned.....	28
Platform Requirements and Design Goals.....	31
3 NOVA 2.1 AIRFRAME.....	35
Wing Design.....	35
Tail Design and Stability Considerations.....	42
Fuselage Design and Center of Gravity Considerations.....	46
Control Redundancy and RDS Linkages.....	48
Avionics.....	50
Power System and Cooling.....	52
Fabrication and Assembly.....	56
Performance Evaluation.....	59
Platform Overview.....	60
Airframe.....	60
Electronics.....	60
Deployment.....	60
4 SYSTEM DEPLOYMENT AND EVALUATION.....	62
ISR Mission Profile.....	62
Photogrammetry Mission Profile.....	63
Flight Planning Implications.....	64

Flight Planning Optimization .....	70
Operational Feasibility of sUAS for Remote Sensing Applications .....	73
5 SPEED TO FLY APPLICATION .....	75
Theory.....	75
Trailing Edge Control .....	79
Initial Power System Model.....	87
Experimental Power Consumption Testing .....	91
STF Application .....	96
Autopilot Integration of Variable Camber for STF .....	103
6 SUMMARY AND CONCLUSIONS.....	107
Summary .....	107
Conclusions .....	108
Recommendations.....	108
LIST OF REFERENCES .....	111
BIOGRAPHICAL SKETCH.....	114

## LIST OF TABLES

<u>Table</u>		<u>page</u>
3-1	Nova 2.1 wing design parameters .....	39
3-2	Nova 2.1 tail design parameters .....	44
3-3	Comparison of motor specifications for Neu 1509-1.5Y and Scorpion 4025-12 .	53
3-4	Comparison of as-built Nova 2 and Nova 2.1 platforms .....	60
5-1	MH32 wing configuration parameters .....	85

## LIST OF FIGURES

<u>Figure</u>	<u>page</u>
1-1 Typical forward and lateral overlap values on adjacent flight lines for aerial photogrammetry missions .....	21
1-2 Nova 2.1 flight planning guide for determining flight line spacing and airspeed for desired overlap.....	22
1-3 Illustration of loss of stereoscopic coverage between (a) uncrabbed adjacent images and (b) overlapping images with crosswind-induced crab angle.....	23
2-1 Failed launch attempt of MLB Foldbat at Pine Island, FL.....	25
2-2 Assembled Tadpole WSUAV.....	26
2-3 Top and side view of completed Nova 1 airframe.....	27
2-4 Assembled Nova 2 sUAS.....	28
2-5 Hand launch and water recovery of Nova 2.1 sUAS from airboat on Lake Okeechobee, FL demonstrating operational constraints imposed by the unique operating environment.....	34
3-1 Drag polar of SD7032 airfoil at cruise and dash average Reynolds numbers of 350k and 700k, respectively.....	38
3-2 Nova 2.1 wing planform with XFLR5 mesh distribution displayed.....	39
3-3 Comparison of lift-to-drag ratios for Nova 2 and Nova 2.1 wing designs.....	40
3-4 Wing bending moment diagram illustrating 85% reduction in bending moment resulting from outboard joiner location.....	41
3-5 Nova 2.1 wing polyhedral configuration in front view.....	42
3-6 Overview of Nova 2.1 tail design.....	45
3-7 XFLR5 streamline analysis illustrating tail placement away from downwash and fuselage junction vortices.....	45
3-8 Preliminary component placement for CG calculations was completed prior to final fuselage design.....	46
3-9 Nova 2.1 complete airframe configuration.....	47
3-10 Schematic of aileron RDS linkage showing tool- and electrical-free connection.....	49

3-11	Tail RDS linkages. ....	50
3-12	Custom machined autopilot enclosure allows for complete waterproofing of critical components while maintaining adequate heat management. ....	51
3-13	Fuselage top populated with electronics prior to joining. ....	52
3-14	Efficiency plots for Neu 1509-1.5Y (inrunner) and Scorpion 4025-12 (outrunner) motor options for 18.5 V input. ....	53
3-15	Propeller efficiencies for various <i>P/D</i> and <i>J</i> ratios. ....	54
3-16	Nova 2.1 propulsion system, with Aeronaut CAM 15x13 folding propeller, externally vented Neu 1509-1.5Y, and Phoenix Ice 100 external heat sink. ....	56
3-17	Local unidirectional carbon reinforcements around wing mounts and hatch locations. ....	57
3-18	Schematic of fuselage halves built with molded-in seam “joggle” ....	58
3-19	Completed fuselage prior to avionics install in preparation for joining. ....	58
3-20	Wing construction picture showing selective local reinforcement with unidirectional and bidirectional carbon fabrics. ....	59
3-21	Disassembled Nova 2.1 illustrating small deployment volume. ....	61
3-22	Assembled Nova 2.1 aircraft. ....	61
4-1	Typical sUAS flight profile for ISR missions. ....	62
4-2	Dipole flight path over areal target on Lake Okeechobee, FL with each point representing a single image exposure. ....	66
4-3	Linear flight path over levee target with takeoff and landing spirals visible. ....	67
4-4	Flight line patterns for remote sensing applications. ....	69
4-5	Flight plan design procedure and relevant parameters. ....	70
4-6	Parallel-track flight plan for mapping road degradation in Picayune Strand State Forest, FL. ....	71
4-7	Flight profile for a typical sUAS-based aerial mapping mission. ....	72
4-8	Optimized flight profile with more aggressive takeoff/climb routing and a power-off descent to landing. ....	73

5-1	XFLR5-generated power curve (assuming 100% propulsion efficiency) for Nova 2.1 illustrating graphical computation of optimal STF in still air. By flying at $V_{mp}$ ( $mp$ = minimum power), power consumption is held at a minimum and maximum duration is achieved. However, flying at $V_{mr}$ ( $mr$ = maximum range), minimizes the Distance Specific Energy Consumption (given by the quotient $P/V$ ) and maximizes the distance traveled per unit of input energy. ....	77
5-2	XFLR5-generated Nova 2.1 power curve illustrating application of STF theory. With a 10 m/s headwind, the tangent line's x-intercept shifts to the right indicating a loss in effective groundspeed and the new optimal airspeed, $V_{mr}$ , is found to be higher than the still air value, $V_{mr}^*$ .....	78
5-3	Visual comparison of SD7032 and MH32 airfoils.....	81
5-4	Comparison of drag polars ( $Re=350k$ ) for original SD7032 and MH32 airfoils. ...	82
5-5	Trailing edge configurations for various flight mode settings. ....	83
5-6	MH32 wing in clean, takeoff, and brake configurations. Camber change is especially noticeable at the inboard flap edges. ....	84
5-7	Computed drag curves for original SD7032 wing and MH32 wing in clean, float and dash modes demonstrating improved performance in high speed cruise.....	86
5-8	XFLR5-generated power curves for original SD7032 wing and composite curve for selected MH32 flight modes. The full selection of flight modes has been omitted for clarity. ....	87
5-9	Power system block diagram.....	88
5-10	Static thrust test results for Neu 1509/1.5Y (6.7:1 GB), Phoenix Ice 100, Aeronaut CAM 15x13 folding prop.....	89
5-11	Comparison of computational power curve model with experimental values for original SD7032 wing. ....	90
5-12	Power testing flight plan consisting of repeated 1.6 km long parallel transects.....	92
5-13	Airspeed intervals for MH32 clean configuration flight.....	93
5-14	Experimentally derived power consumption results compared for original Nova 2.1 wing and modified MH32 configurations.....	94
5-15	Airspeed intervals for SD7032 configuration flight showing much noisier data and a climb fault occurring during a 24 m/s transect. ....	95

5-16	Variation of advance ratio, $J$ , across airspeed range for MH32 clean configuration. ....	96
5-17	Experimentally obtained MH32 power curve with still air DSEC shown.....	97
5-18	Schematic of flight performance for 2 km transects in still air conditions detailing time of flight and power consumption. ....	98
5-19	Schematic of flight performance for 2 km transects in 10 m/s steady wind conditions, illustrating efficiency losses without STF application. ....	99
5-20	Improved time and ground coverage efficiencies for 2 km transects in 10 m/s steady wind with STF application. ....	100
5-21	Demonstration of performance gains using variable camber enhanced STF on MH 32 composite power curve. ....	101
5-22	Schematic of flight performance with variable camber enhanced STF application. ....	102
5-23	Positive feedback in closed-loop flap control. ....	105

## LIST OF ABBREVIATIONS

A	Ampere
Ah	Ampere-hour
AR	Aspect Ratio
$b$	Wingspan
cc	Cubic Centimeter
CCD	Charge-Coupled Device
CG	Center of Gravity
CIR	Color Infrared
$C_d$	Section Drag Coefficient
$C_l$	Section Lift Coefficient
$C_{l,max}$	Section Maximum Lift Coefficient
$C_{L,max}$	Wing Maximum Lift Coefficient
cm	Centimeter
COTS	Consumer Off-The-Shelf
$D$	Propeller Diameter
DEM	Digital Elevation Model
dm	Decimeter
D-SLR	Digital Single Lens Reflex
DSEC	Distance Specific Energy Consumption
EDA	Equivalent Dihedral Angle
ESC	Electronic Speed Control
FAA	Federal Aviation Administration
g	Gram
gsm	Grams per Square Meter

GCP	Ground Control Point
GCS	Ground Control Station
GPS	Global Positioning System
HALE	High Altitude, Long Endurance
Hz	Hertz
IMU	Inertial Measurement Unit
INS	Inertial Navigation System
ISR	Intelligence, Surveillance, and Reconnaissance
ITAR	International Traffic in Arms Regulations
<i>J</i>	Propeller Advance Ratio
kg	Kilogram
km	Kilometer
kV	Rotations per Minute per Volt
<i>L/D</i>	Lift-to-Drag Ratio
m	Meters
MAC	Mean Aerodynamic Chord
mAh	Milliampere-hour
MAV	Micro Air Vehicle
mi	Mile
MP	Megapixel
m/s	Meters per Second
<i>n</i>	Revolutions per Minute
N	Newton
N-m	Newton-meter
<i>P</i>	Power

$P/D$	Propeller Pitch-to-Diameter Ratio
PID	Proportional-Integral-Derivative
$P_{min}$	Minimum Input Power
RDS	Rotary Drive System
Re	Reynolds Number
RF	Radio Frequency
$R_{min}$	Minimum Turn Radius
RMS	Root Mean Squared
RPM	Revolutions per Minute
S	Wing Area
sUAS	Small Unmanned Aerial System
STF	Speed to Fly
UAS	Unmanned Aerial System
UASRG	Unmanned Aerial Systems Research Group
UAV	Unmanned Aerial Vehicle
UF	University of Florida
USACE	US Army Corps of Engineers
V	Volt
$V$	Airspeed
VLOS	Visual Line of Sight
$V_{mp}$	Minimum Power Airspeed
$V_{mr}$	Maximum Range Airspeed
W	Watt
Wh	Watt-hour
WS	Wingspan

$W/S$

Wing Loading

$\rho$

Air Density

$\theta_t$

Tail Dihedral Angle

Abstract of Thesis Presented to the Graduate School  
of the University of Florida in Partial Fulfillment of the  
Requirements for the Degree of Master of Science

IMPROVING OPERATIONAL EFFICIENCY OF SMALL UNMANNED AIRCRAFT  
SYSTEMS FOR REMOTE SENSING APPLICATIONS

By

Brandon Scott Evers

December 2011

Chair: Peter Ifju

Major: Aerospace Engineering

Aerial photogrammetry is traditionally a specialized application for small manned aircraft with large operating expenses. Emerging small unmanned aerial systems (sUAS) have the capability to augment existing manned missions with low-level, cost effective unmanned missions. One of the main barriers to the use of sUAS is their limited endurance with current propulsive methods. To optimize data post-processing, care should be exercised to ensure that images are taken orthogonal to the direction of the flight path. To minimize crosswind-induced crab angles, flight paths should always be flown directly into or with the wind, thus simplifying the wind interaction to a purely additive or subtractive term for ground coverage. Thus, neglecting turns and altitude changes, the optimization problem is simplified to total ground coverage with vehicle speed and wind speed as the only variables. With this flight regime determined prior to vehicle construction, optimal range can be increased by the inclusion of trailing edge (camber/reflex) control, maximizing the Lift to Drag ratio ( $L/D$ ) to minimize power consumption over a range of airspeeds. The results presented here couple aerodynamic analysis, ground coverage efficiency, and power consumption data to provide a method for calculating optimal flight speeds in any given wind condition for

maximum coverage. Due to the complex interaction between the aerodynamic and propulsive efficiencies of the sUAS, interesting and non-intuitive results emerge. In an approach analogous to the speed-to-fly theory used in cross-country soaring, a dynamic flight management algorithm was developed on a modified Procerus® Kestrel™ autopilot. This algorithm allows the sUAS to monitor the winds aloft and modify the flight plan transects and commanded airspeeds accordingly. Furthermore, this algorithm sets the camber of the airfoil at its optimum position for each portion of the flight plan. This combination of orientation, commanded airspeed, and camber position maximizes the total area mapped per flight. Initial tests of the flight management algorithm yielded significant improvements in ground coverage efficiency in terms of both energy consumption and required flight time. By reducing energy and flight time requirements by up to 14% and 43%, respectively, these flight management strategies significantly improve the operational feasibility of sUAS for remote sensing applications.

## CHAPTER 1 INTRODUCTION

### **Motivation**

High precision mapping and engineering products produced using aerial photogrammetry techniques have typically been serviced by small manned aircraft deploying large frame cameras coupled with expensive inertial and geolocation equipment (Wolf and Dewitt 2000). However, recent advances in the quality of small optical sensors and inertial navigation equipment have led to the adoption of small unmanned aerial vehicles (UAVs) as a platform for remote sensing applications. By directly georeferencing the imagery as it is captured, analysts can later construct high-accuracy digital elevation models (DEMs) and mosaicked orthophotos acceptable for a wide range of environmental, engineering, and management applications (J. H. Perry 2009). Because this imagery can be processed without the requirement of presurveyed ground control points (GCPs), data collection can proceed much faster than traditional methods and in areas previously unreachable for the survey of GCPs. An additional advantage is found in the low operating altitudes of sUAS for remote sensing, which enable the collection of very high-resolution imagery (sub 1-cm pixel size) which traditional platforms cannot readily achieve. Finally, the acquisition, mobilization, and deployment costs associated with sUAS are much lower than those of traditional platforms, which places remote sensing data in the hands of more engineers and researchers and permits more frequent acquisitions, further increasing their scientific value.

## **The UF Nova Project**

For more than a decade, interdisciplinary researchers at the University of Florida (UF) Unmanned Aircraft Systems Research Group (UASRG) have advanced an interdisciplinary project to investigate and refine techniques to utilize sUAS for remote sensing applications (Jones 2003). While early efforts were focused on real-time video-based payloads for wildlife monitoring, a programmatic shift towards production of high-accuracy, high-resolution orthomosaics developed, motivated by the increased number of applications for this data type (Wilkinson 2007).

While real-time video streams are valuable for immediate awareness during situations like wildfire monitoring and natural disaster response, the vast majority of natural resource applications require high-accuracy high-resolution imagery over large geographic areas. Although hours of full motion video can yield the same information about a given target area, the resulting deluge of data, its storage and subsequent processing put it at an operational disadvantage to the at-a-glance situational awareness afforded by still orthomosaics (Magnuson 2010).

Additionally, for projects involving traditional remote sensing postprocessing techniques like automated vegetation classification, current methods are optimized for utilization of still imagery (Jensen 2004). The high-resolution imagery products able to be produced by an sUAS-based data collection system yield themselves to a variety of applications, from vegetation imaging for crop assessment, (MacArthur, Schueller and Crane 2005), environmental rehabilitation (Nyquist 1996), habitat evaluation (Breckenridge, Harbour, et al. 2006), and rangeland monitoring (Breckenridge 2007). In addition to research-focused deployments of the technology, potential operational applications for invasive species mitigation, infrastructure inspection, and environmental

impact monitoring attracted additional support from the US Army Corps of Engineers (USACE), Jacksonville District (Bowman, Watts, et al. 2008).

As a result, an evolving focus of the project became the advancement of the system technology for data collection and processing to the point where operators external to the UASRG development team could reliably produce scientifically usable data on a repeatable basis (Burgess, Ifju, et al. 2009). This operational requirement, relatively unique for a research organization, has led to a number of developmental advantages that would not otherwise have been encountered (Vorse 2011).

### **Directly Georeferenced Aerial Photogrammetry**

Using directly georeferenced aerial imagery, geomaticists can produce highly accurate orthomosaics and DEMs by using an aerotriangulation process. At its core, direct georeferencing refers to the tagging of each image with a set of exterior orientation parameters (EOPs), estimated camera position and orientation data given by an INS/GPS (J. H. Perry 2009). Through multiple observations of common tie points between adjacent images, aerotriangulation is then used to improve the fidelity of those initial estimations. These improved EOPs are then used to create a geometric model of the terrain needed for accurate mosaicking of the overlapping images. Because the EOPs are used to compute the scene geometry and vice versa, a simultaneous bundle adjustment is performed, which combines the two models and performs a least-squares minimization on the estimation error (Wolf and Dewitt 2000). This simultaneous bundle adjustment is one of the key advantages of the photogrammetric technique, as it enables the accuracy of the completed DEMs and orthomosaics to be improved over the initial accuracy of the raw INS/GPS sensor data.

The overall time required to complete this lengthy processing technique can be minimized by improving the accuracy of the initial parameter estimates, which requires sufficient coverage of the target area by multiple observations. Full stereoscopic coverage, needed for generation of 3D scene geometry, requires that every point in the target area be imaged at least twice. To guarantee sufficient coverage, minimum image overlaps between adjacent exposures must be maintained both along flight lines and across adjacent lines. As shown in Figure 1-1, forward overlap (endlap) and lateral overlap (sidelap) refer respectively to the percentage overlaps between images along the same flight line or on adjacent lines while forward and side airbase refer to the respective spacing between adjacent images.

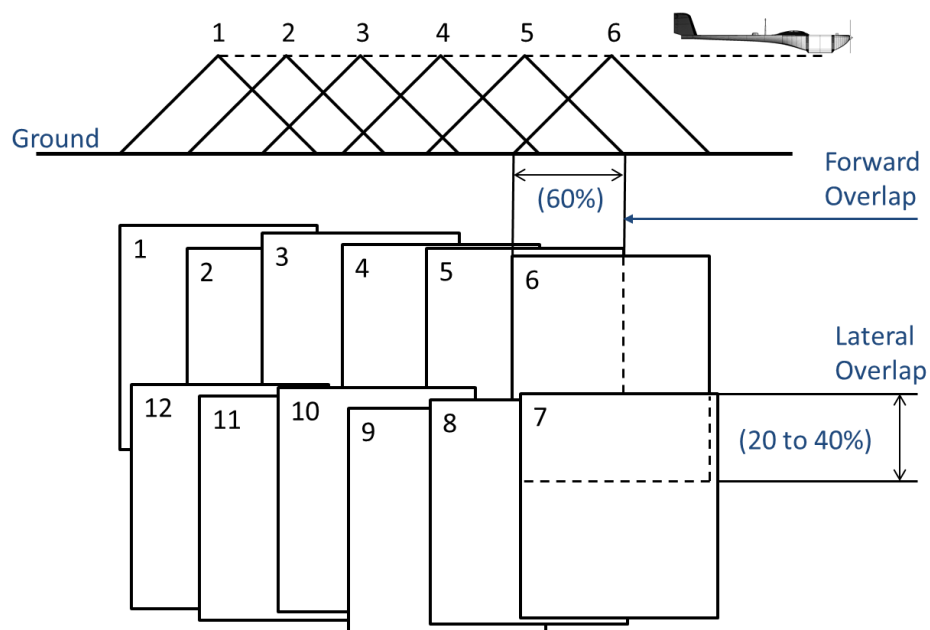


Figure 1-1. Typical forward and lateral overlap values on adjacent flight lines for aerial photogrammetry missions.

While camera parameters like the interval between exposures, lens focal length, and sensor geometry contribute to determining image overlap, flight parameters like spacing between adjacent flight lines, altitude, and airspeed also have definite effects.

For most flights with the Nova project payload, altitude is primarily dictated by desired output resolution (flying lower for higher resolution), leaving airspeed and flight line spacing to be determined to maintain desired endlap and sidelap percentages. For a given set of camera parameters, a flight planning guide can be developed to determine appropriate values for these parameters with overlap requirements based on desired output products. A sample flight planning guide for the current Nova 2.1 payload is shown in Figure 1-2 (J. H. Perry 2009).

					Altitude (m)											
43	86	130	173	400	93%	91%	90%	86%	84%	83%	81%	79%	77%	76%	74%	3D Coverage
41	81	122	162	375	93%	91%	89%	85%	83%	81%	80%	78%	76%	74%	72%	
38	76	113	151	350	92%	90%	88%	84%	82%	80%	78%	76%	74%	72%	70%	
35	70	105	140	325	91%	89%	87%	83%	81%	79%	76%	74%	72%	70%	68%	
32	65	97	130	300	91%	88%	86%	81%	79%	77%	75%	72%	70%	68%	65%	
30	59	89	119	275	90%	87%	85%	80%	77%	75%	72%	70%	67%	65%	62%	
27	54	81	108	250	89%	86%	83%	78%	75%	72%	69%	67%	64%	61%	58%	2D Mosaic
24	49	73	97	225	88%	85%	81%	75%	72%	69%	66%	63%	60%	57%	54%	
22	43	65	86	200	86%	83%	79%	72%	69%	65%	62%	58%	55%	51%	48%	
19	38	57	76	175	84%	80%	76%	68%	64%	60%	56%	52%	48%	44%	40%	
16	32	49	65	150	81%	77%	72%	63%	58%	54%	49%	44%	40%	35%	31%	
14	27	41	54	125	78%	72%	67%	56%	50%	44%	39%	33%	28%	22%	17%	Individual
11	22	32	43	100	72%	65%	58%	44%	38%	31%	24%	17%	10%	3%	-4%	
8	16	24	32	75	63%	54%	44%	26%	17%	7%	-2%	-11%	-20%	-30%	-39%	
5	11	16	22	50	44%	31%	17%	-11%	-25%	-39%	-53%	-67%	-81%	-94%	-108%	
3	5	8	11	25	-11%	-39%	-67%	-122%	-150%	-178%	-206%	-233%	-261%	-289%	-317%	
80%	60%	40%	20%		8	10	12	16	18	20	22	24	26	28	30	
Sidelap %				Groundspeed (m/s)												

**Instructions:**

1. Calculate groundspeed = programmed airspeed + observed wind
2. Select altitude based on desired endlap using the right side of the table
3. Select flight line spacing distance on the left side of the table based on desired sidelap percentage

Figure 1-2. Nova 2.1 flight planning guide for determining flight line spacing and airspeed for desired overlap. [Adapted from Perry, J.H. 2009. A Synthesized Directly Georeferenced Remote Sensing Technique for Small Unmanned Aerial Vehicles. Master's Thesis (Page 82, Figure 4-11). University of Florida, Gainesville, FL.]

A major factor in flight planning for sUAS is the direction and intensity of winds aloft. Changes to vehicle groundspeed as a result of the wind's additive effects to airspeed must be accounted for to ensure that endlap requirements are met. Because the Nova 2.1 payload does not have an azimuthal mount to continuously correct for

crosswind-induced sideslip, significant losses in stereoscopic coverage can occur when the aircraft heading is not in line with the ground track, as shown in Figure 1-3. As a result, it is most efficient for flight lines to be oriented in-line with prevailing winds to minimize potential coverage losses due to this sideslip, or crab.

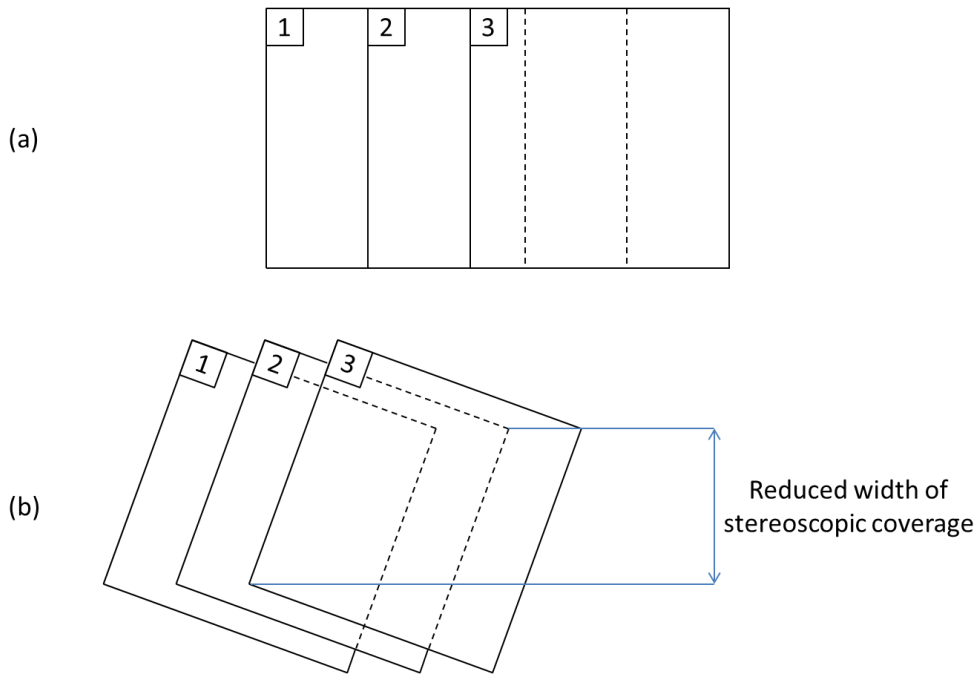


Figure 1-3. Illustration of loss of stereoscopic coverage between (a) uncrabbed adjacent images and (b) overlapping images with crosswind-induced crab angle.

## CHAPTER 2 NOVA PROJECT PLATFORM DEVELOPMENT

### **Legacy Systems**

Since 2001, the UF UASRG has fielded 5 generations of sUAS, with each successive iteration building upon lessons learned from deployments of previous generations. A programmatic feedback loop was created wherein increasingly reliable and capable airframes enabled the development of more sophisticated payloads that delivered increasingly valuable data products. The emergent demand for increased geographic coverage with these improved data deliverables then drove the push for further improving airframe deployability and endurance, completing the cycle and beginning a new generational loop.

The program's initial sensor platform was the FoldBat, a commercial offering from the MLB Company. With a 1.5 m wingspan and a flying weight of 4.3 kg, the FoldBat deployed a trio of 330-line CMOS cameras, transmitting live video to a ground station for tracking and recording. The low resolution provided by these chip imagers soon motivated a payload modification to a single 525-line progressive scan camera, at the expense of increased payload weight. Propulsion was provided by a nitromethane-fueled 5.2cc glow engine, which yielded 45 minutes of endurance. Unfortunately, the high wing loading of the FoldBat led to poor takeoff and landing success rates, especially during field operations from challenging launch sites, as seen in Figure 2-1. Additionally, the lightweight airframe's fragility and lack of waterproofing made it unsuitable for operation in wetlands and marine areas targeted for study by the research group (Jones 2003).



Figure 2-1. Failed launch attempt of MLB Foldbat at Pine Island, FL.

To address the operational deficiencies of the FoldBat system, members of the UF Micro Air Vehicles (MAV) Lab developed the Tadpole, an electrically powered sUAS designed for wildlife surveillance (Lee 2004). The resulting 2 m wingspan, 3.4 kg Tadpole, shown in Figure 2-2, carried two CCD cameras (nadir and side-look) with an onboard digital video recorder. While much more successful during field deployments than the FoldBat, the Tadpole's limited 30 minute flight endurance and lack of adequate geolocation for the captured video data motivated development of a subsequent platform (Wilkinson 2007).



Figure 2-2. Assembled Tadpole WSUAV.

The resulting Polaris/Nova 1 system was developed expressly to provide accurately georeferenced imagery and the overall system architecture began to reflect that developing mission (Bowman 2008). Built on a modified Tadpole fuselage, the 2.44 m wingspan Nova 1, shown in Figure 2-3, boasted an onboard payload control computer that combined images from a stripped-down 12.1 MP Canon point-and-shoot still camera with GPS position and orientation metadata from the autopilot IMU. Although limited by the low precision and update rates of the metadata, this direct georeferencing enabled limited photogrammetric post-processing of the imagery to permit geolocation of visible targets with a 67.6 m RMS error (Bowman 2008). The success of the Nova 1 system in producing directly georeferenced imagery from an sUAS led to a development effort intended to push the technology to an operational phase where deployment crews from the USACE and similar organizations could repeatably and reliably collect georeferenced imagery for a variety of projects.



Figure 2-3. Top and side view of completed Nova 1 airframe.

To accomplish this goal, a dramatically improved photogrammetric payload was developed by the geomatics team of the UF UASRG. The new payload, designed to use commercial off-the-shelf (COTS) components, centered around an Olympus® E-420 digital single lens reflex (D-SLR) camera, which offered a much larger sensor and improved optics over previous imagers. To deliver improved navigation and sensor orientation data, an Xsens MTi-G GPS/INS was selected, offering major improvements in both accuracy and update rate over the relatively coarse sensors used by the autopilot. This is key for improving photogrammetric processing because at a flying height of 200 m, a 3 degree error in the estimated orientation of the camera results in a 10.5 m error in the initial positional estimate. This ultimately results in increased search spaces and dramatically longer processing times. (J. H. Perry 2009). Additionally, the MTi-G is not subject to cumbersome International Traffic in Arms Regulations (ITAR), meaning that both the physical deployment of the device and its collected data are not ITAR-restricted and more readily publishable.

The Nova 2 platform was a significantly larger aircraft than its predecessors, maintaining the 2.44 m wingspan of the Nova 1, but enlarging the planform area and fuselage to present a much larger aircraft better suited to the increased space

requirements of the upgraded payload. As indicated by the USACE logo and paint scheme on the Nova 2 airframe in Figure 2-4, the Nova 2 was the first sUAS to successfully demonstrate the operational deployment of a UF UASRG-developed system by external operators. In moving the deployment of the platform from a research and development stage into this new operational phase, a unique set of associated design challenges were presented (Burgess, Percival, et al. 2009).



Figure 2-4. Assembled Nova 2 sUAS.

### **Lessons Learned**

Although relatively successful as an initial test/deployment platform for the current generation mapping payload, there were a number of significant design and operational issues with the Nova 2 system. To realize the program's stated goal of operational system deployment by non-expert operators external to the UF development team, the platform reliability needed to be enhanced and the overall assembly and deployment

simplified. Additionally, research flights focused on operational procedure optimization required a stable platform whose reliability was never in question.

The key flaw in the Nova 2 design was excessive platform weight. With a wingspan of 2.44 m and a planform area of 67.4 dm<sup>2</sup>, the Nova 2 tipped the scales at 5.1 kg without payload and 6.1 kg with a typical loadout supporting a single E-420 D-SLR. Neglecting payload, this was already in excess of the 4.5 kg design weight around which the wing area was optimized and is mostly attributable to inefficient laminate design and manufacturing techniques. For expediency, the entire vehicle was constructed of a laminate of carbon fiber fabric with an epoxy matrix. The fuselage was hollow molded with three layers of 190 gsm bidirectional carbon fabric while the foam-core wing was reinforced with a single vacuum-bagged layer of 190 gsm bidirectional carbon fabric. While strong, this layup schedule resulted in a heavier than necessary airframe that was also brittle during landing recoveries on unimproved fields. Additionally, because carbon fiber is a conductor, significant RF interference and blanking was encountered during flight testing due to the aircraft's structure shadowing of the RF link between the ground station and the airborne vehicle.

Inadequate early collaboration between airframe and payload specialists also meant that the airframe was delivered without consideration of payload location and its effect on the aircraft's center of gravity (CG) location. As a result, the optimal operational configuration resulted in the Nova 2 being severely nose-heavy, which, when combined with the offset thrust line and high wing loading, contributed to a number of failed hand launch attempts.

As a result of the Nova 2's overweight operational condition, the flight performance of the platform suffered. This was especially evident in the vehicle's poor takeoff and landing performance, owing to the high stall speed of 17 m/s. This is a relatively high value for platforms in this size class, especially for hand-launched, belly-landed aircraft, and led to numerous operational incidents during these flight phases.

An additional consequence of the increased flying weight was the Nova 2's minimum cruise airspeed of 22 m/s, which was found to be too high to achieve the minimum specified airbase at lower altitudes, making all downwind legs practically worthless for effective data collection. For operational deployments, such a large effective loss is critical as it halves potential ground coverage per flight, minimizing the vehicle's practical effectiveness compared to alternate remote sensing methods. Also negatively impacting the Nova 2's operational effectiveness was its poor mission endurance, with typical flight durations of 35 minutes. Coupled with the platform's long turnaround time between missions, this severely limited the amount of ground coverage a crew could achieve per day.

Finally, from a practical deployment perspective, a number of critical design flaws hampered the Nova 2's effectiveness as a reliable data collection platform. First, water intrusion proved to be a major issue during wetlands missions, contributing to at least one terminal in-flight failure. Numerous ingress points at mechanical junctions like the fuselage/boom joint and wing and tail mating surfaces as well as cooling inlets around the motor were inadequately sealed, leading to significant accumulation of water in the fuselage and subsequent elevator servo failure during operations on Lake Okeechobee, FL. Additionally, insufficient cooling of electronics was found to be an issue, with the hot

operating environment and waterproof enclosure requirements compounding the situation. As a result, poor reliability was encountered, with an emergency flight recovery required on one mission due to an in-flight ESC fire. Lastly, field assembly and preflight procedures for the vehicle were cumbersome and time-consuming, a situation frequently exacerbated by the frequent requirement to remove and refit the wing or front hatch to reset a preflight system fault. Removing the wing required the replacement of 14 rubber bands used to mount the wing, while front hatch access demanded replacing a taped seal needed to waterproof the fuselage, neither task a welcome one on the deck of an airboat.

### **Platform Requirements and Design Goals**

As a result of lessons learned during initial operational deployments of the Nova 2 system, a refined platform design was deemed necessary, with a number of key performance criteria guiding the design. First among which, and a key lesson in overall sUAS work, is to begin vehicle design by evaluating what data product is to be produced with the system. Almost all sUAS research programs begin with an available platform which program managers then try to adapt to their specific needs, while often being handicapped by the system's initial ISR-focused development (Owen 2011). Instead, program managers should determine who will be using the resulting data products and consult with the end users to determine ultimate delivery data specifications. From there, appropriate payload design and specifications should be developed, along with the payload's operational requirements. These operational specifications can include the need for a gyro-stabilized gimballed camera, a hovering requirement for persistent observation, high altitude operations, etc. Once a suitable payload is determined, vehicle design should then proceed to maximize payload

effectiveness and the overall mission feasibility through range and duration maximization. Moreover, to improve flexibility in deployment logistics, the platform should be designed to enable operation with a minimum of runway, launcher, and recovery areas and equipment.

With this process in mind, design of the Nova 2.1 began with determining what payload configuration would maximize mission effectiveness for the natural resource and infrastructure monitoring missions that the program sought to execute. To deliver the high-accuracy, high-resolution orthomosaics identified as key deliverables, the payload developed for this aircraft is deployed in a 'strapdown' configuration, meaning that the camera is affixed to the fuselage and therefore has the same heading and orientation as the aircraft. To ensure sufficient overlap for full photogrammetric coverage, this requires that the payload be maintained in a near-constant nadir view while over the target area.

In addition to specific payload deployment needs, remote sensing applications similarly call for specialized vehicle requirements. For example, typical Intelligence, Surveillance, and Reconnaissance (ISR) missions require maximum duration on target and normally remain at a fixed airspeed except during brief dash periods as required by the mission. As a result, vehicle optimization centers on maximizing duration, typically at a low cruise airspeed to minimize power consumption and enable the vehicle to orbit compact target areas. However, remote sensing applications focus on maximizing total ground coverage per flight to minimize operational downtime between flights, which heavily influences the amount of area covered by a single flight crew per day. Also, the desired airspeed is completely dependent on the imagery product specifications, and

may range from a very low speed required to guarantee overlap for low-altitude high-resolution studies to a high cruise speed intended to minimize redundant data for higher-altitude medium-resolution flights. Drawing on the lessons learned from deployment of the Nova 2, a minimum cruise speed of 15 m/s was determined to adequately fulfill the minimum forward overlap required by the system's 2.5s interval between exposures at a 150m altitude.

Many remote sensing applications for environmental monitoring purposes involve operating in rugged terrain where suitable launch and recovery sites may be unavailable. As a result, the Nova 2.1 platform specifications were developed cooperatively with the USACE and the geomatics specialists at UF to provide a small, hand-launched sUAS able to be launched and recovered from an airboat operating in the swamps and waterways of South Florida, as shown in Figure 2-5. These capabilities, unique to the Nova series of aircraft, improve operational availability without the additional complexity of custom launch and recovery equipment or location requirements. Inherent in the hand launch requirement is a sufficiently low stall speed to minimize failed launch events, which are common to many marginally hand-launchable systems. Additionally, reliable repeated operation following water recoveries was targeted as a key goal, which emphasized waterproofing of the fuselage, as well as redundantly waterproofing all of the avionics and 'mission-critical' electronics necessary for safe operation and recovery of the vehicle. Finally, a push for operational simplicity lead to a requirement for simple, tool-free field assembly and readily accessible components for possible troubleshooting in the field.



Figure 2-5. Hand launch and water recovery of Nova 2.1 sUAS from airboat on Lake Okeechobee, FL demonstrating operational constraints imposed by the unique operating environment.

CHAPTER 3  
NOVA 2.1 AIRFRAME

**Wing Design**

In order to obtain the desired flight characteristics established by the UASRG's design goals, a key focus in the development of the Nova 2.1 wing design was the reduction of wing loading ( $W/S$ ). Although optimal airfoil selection and planform design can enhance the wing's overall efficiency, there are definite limits to these optimizations if the base design is not within an acceptable window. For critical phases of flight like takeoff and landing, wing loading is a primary factor in determining minimum stall speed, according to Equation 3-1.

$$V_{stall} = \sqrt{\frac{2(W/S)}{\rho C_{L,max}}} \quad (3-1)$$

Additionally, wing loading determines how hard the wing is working during cruise, with lightly loaded wings having more efficient cruise performance at low speeds than designs with higher wing loadings (Anderson 2007). Turn performance is also affected, which is a key factor affecting mission planning for remote sensing applications. Given by Equation 3-2, the minimum turn radius ( $R_{min}$ ) an aircraft can perform at a given bank angle,  $\theta$ , is directly proportional to its wing loading; that is, lightly loaded wings can perform tighter turns.

$$R_{min} = \frac{2(W/S)}{\rho C_L \sin \theta} \quad (3-2)$$

Finally, reducing the design wing loading helps alleviate some of the “weight growth” issues inherent in aircraft development. Because additional features and equipment inevitably find their way into the airframe, conservatively low design wing loadings help to reduce subsequent losses in takeoff and turn performance as weight is added until the final configuration is reached.

Because the Nova 2.1 would deploy an existing photogrammetric payload already developed for the Nova 2, the maximum payload weight could be readily calculated. To provide mission flexibility, the additional weight of a second E-420 imager was accounted for in the event that simultaneous capture of color infrared (CIR) imagery or deployment of an alternate auxiliary sensor was dictated by mission requirements. With the maximum payload weight established, an initial vehicle weight estimate was determined by selecting approximate flight component weights and estimating total laminate weights for the wings, fuselage, and tail. Solidworks was used to determine surface area in order to compute laminate weight using estimated layup schedules. This resulted in an estimated maximum vehicle weight of 5.9 kg.

Because the USACE did not want to increase pilot workload, flaps were omitted, minimizing operational complexity at the cost of overall flight performance.

Unfortunately, without flaps to increase the wing’s overall maximum lift coefficient,  $C_{L,max}$ , the wing design must be focused on maintaining hand-launchability, at the cost of a reduction in absolute cruise efficiency. In order to maintain an acceptably low stall speed to permit easy hand-launching, the wing design must carry higher than normal planform area than if it were designed around a cruise operating point. This excessive

area causes higher parasitic drag, which reduces flight efficiency, especially at higher cruise airspeeds.

The initial wing design, including planform and airfoil optimization, was performed using XFLR5 software, which utilizes a hybrid 3D-panel/vortex lattice method (Deperrois 2011). Minimization of required wing area for takeoff motivated the selection of an airfoil with a relatively high section  $C_{l,max}$ . To achieve this high section  $C_{l,max}$  while retaining a relatively thin profile for higher speed cruise at lower  $C_l$  values, a Selig-Donovan SD7032 airfoil (M. S. Selig 1989) was selected. Designed to provide high performance in a low Reynolds number ( $Re \approx 350k$  at cruise) regime, the SD7032 has a low thickness (characteristic of low  $Re$  airfoils) of 9.96% and a camber of 3.66%. This relatively high amount of camber results in a  $C_{l,max}$  of 1.45 and a minimum drag  $C_d$  of 0.45, with the section drag polar presented in Figure 3-1. This minimum drag  $C_d$  is typically a strong indicator of the airfoil's design point, an operating regime in which its optimal performance is reached (Abbott and Von Doenhoff 1959). This value is normally used by designers to select airfoils based on their cruise lift requirements or inversely, to determine optimal operating speeds for a given wing design.

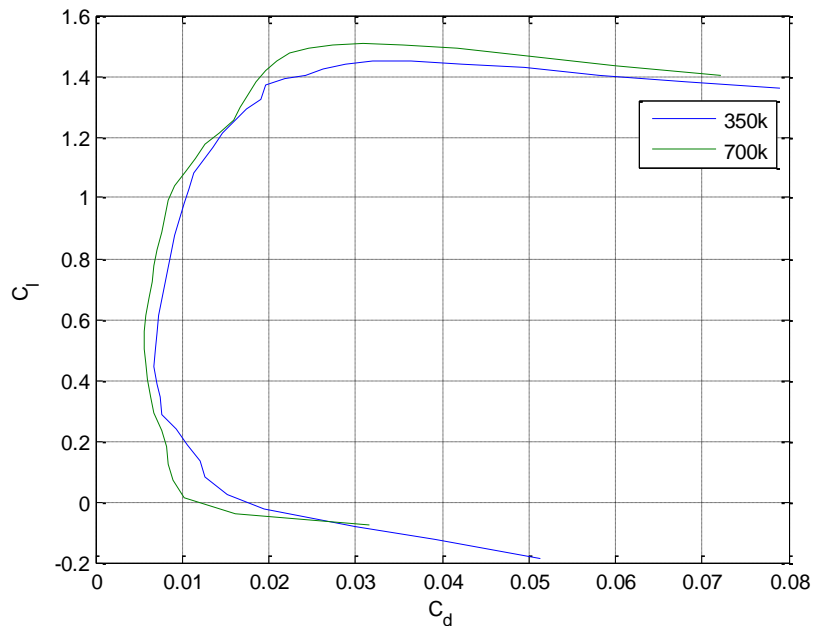


Figure 3-1. Drag polar of SD7032 airfoil at cruise and dash average Reynolds numbers of 350k and 700k, respectively.

Because of the hand-launch requirement, a low minimum stall speed of 12 m/s at maximum weight (10 m/s at typical loadout) was selected to maximize launch success rates during field deployments. Using this minimum stall speed and the airfoil's  $C_{l,max}$ , the resulting design wing area was calculated as 81.5 dm<sup>2</sup>. Although a high aspect ratio wing is desirable to enhance overall efficiency by reducing induced drag, especially at cruise, the Nova 2.1 was constrained to a 2.74 m span for storage and transport purposes, resulting in an aspect ratio of 9.2.

With the overall geometry set, the planform design was then revised to shape the lift distribution toward a near-elliptical arrangement. Because the wing would be constructed using hot-wired foam cores, which only permit straight-tapered trapezoidal panels, a six-panel planform was selected as a compromise to allow sufficient control over lift distribution while minimizing fabrication complexity. At the outer stations, the

SD7032 airfoil was progressively thinned to 8.49% thickness and decambered to 2.98% to provide aerodynamic washout while one degree of geometric washout was also incorporated. Thinning the airfoil towards the tips helps to prevent premature separation due to the lower Reynolds numbers that result from narrower chord widths at these locations. These modifications allow the wing's operating condition to move towards a more elliptical lift distribution while preventing the tips from being too small, which would negatively affect tipstall characteristics as well as create section efficiency losses due to low Reynolds number effects.

The overall wing design is presented in Figure 3-2, with key design parameters reviewed in Table 3-1.

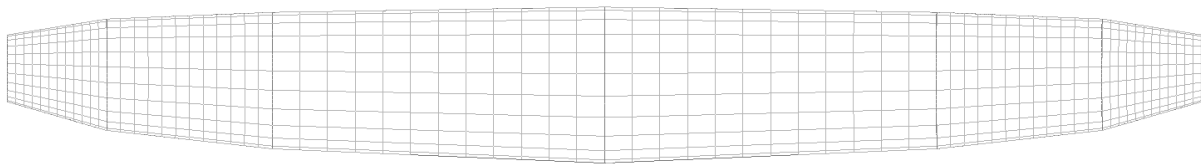


Figure 3-2. Nova 2.1 wing planform with XFLR5 mesh distribution displayed.

Table 3-1. Nova 2.1 wing design parameters

Wingspan, $b$	2.74 m
Planform Area, $S$	81.6 dm <sup>2</sup>
Design Max Wing Loading, $W/S$	7.23 kg/m <sup>2</sup>
Mean Aerodynamic Chord	30.6 cm
Aspect Ratio, $AR$	9.2
Taper Ratio	2.33
Root-Tip Sweep	0.53°

The overall wing performance was evaluated using a fixed-lift polar analysis within XFLR5. The lift-to-drag ratios ( $L/D$ ) for both the Nova 2 and Nova 2.1 are presented in Figure 3-3. For simplicity in comparing wing designs, the fuselage and tails were not included in this analysis, but were later simulated for more accurate performance

assessments. As a result, the computed  $L/D$  ratios are higher than actually encountered in flight, but are still valuable for relative comparison. From inspection, the overall benefit from the increased span and lower wing loading is evident in the Nova 2.1's higher efficiency at lower speeds. Additionally, a reduction in stall speed can be seen in the new design, as well as a downward shift in the maximum efficiency cruise airspeed. Also evident, however, is the inevitable tradeoff in high speed cruise performance, which manifests itself in the Nova 2's superior performance when flying faster than 21 m/s.

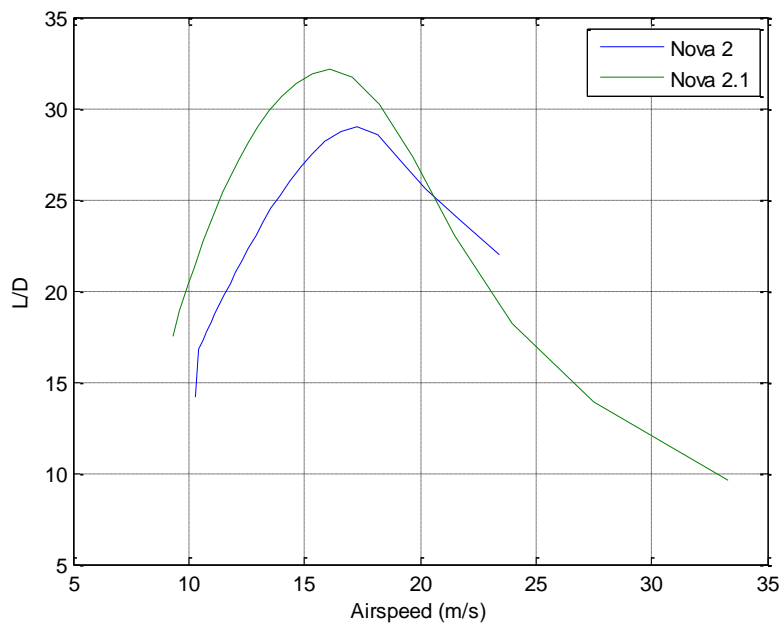


Figure 3-3. Comparison of lift-to-drag ratios for Nova 2 and Nova 2.1 wing designs.

A three-piece wing arrangement was selected to enhance portability while minimizing the wing's structural weight at the panel joiners. As evidenced in the wing bending moment diagram in Figure 3-4, at cruise, moving the wing joiner position from the center station (as in a 2-piece wing) to the first panel break, located 76.2 cm from the root (3-piece wing configuration) results in an 85% reduction in wing bending

moment from 13.7 N-m to 2.1 N-m. This allows for dramatically lighter reinforcement around the wing joiner areas, resulting in simplified construction and structural weight reduction. This also aids in waterproofing during field assembly, as there is no longer a wing joint centrally located over the fuselage to be repeatably and reliably waterproofed with each setup.

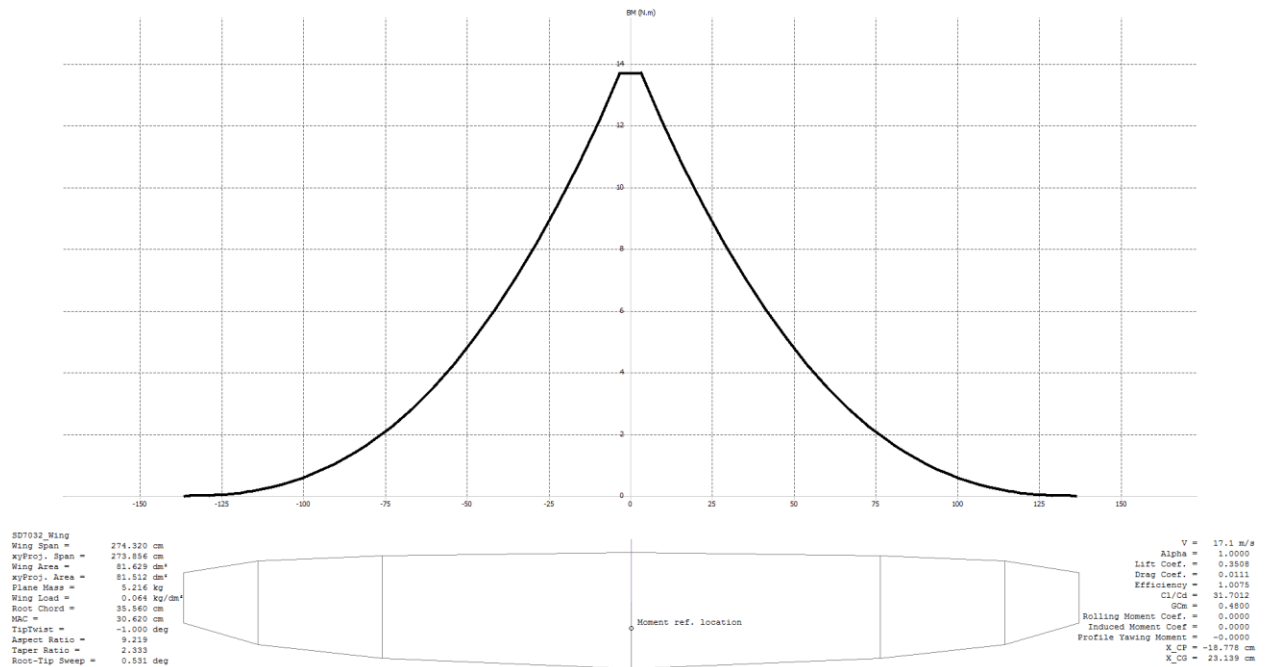


Figure 3-4. Wing bending moment diagram illustrating 85% reduction in bending moment resulting from outboard joiner location.

To provide adequate static stability about the roll axis, polyhedral was incorporated into the wing design, with a flat center section and the outer wing panels raised to 5° as seen in Figure 3-5. This results in an Equivalent Dihedral Angle (EDA) of 2.86°. While modest, this is sufficient to provide adequate proverse roll response to yaw inputs, which allows for effective control redundancy in the event of aileron failure. An unplanned evaluation of this redundancy was encountered during a high-speed power consumption flight, during which both aileron linkages failed, leaving the undriven

ailerons to flutter uncontrollably. Despite the complete loss of direct roll control, adequate orientation and directional control was maintained using only rudder input, and a safe centerline landing was achieved.



Figure 3-5. Nova 2.1 wing polyhedral configuration in front view.

### **Tail Design and Stability Considerations**

One of the design lessons imparted by the field deployment of the previous Nova 2 platform was the structural vulnerability presented by a T-tail configuration during rough landings. The combined vertical impact and horizontal deceleration loads typical of off-field landings were exacerbated by the structural weight of the horizontal stab being located far from the junction between the vertical fin and the tail boom. As a result, frequent fractures occurred at this junction, as well as at the stab attachment points on top of the fin.

An alternate V-tail configuration was selected due to a number of practical, structural, and aerodynamic reasons. Operationally, the V-tail configuration raises the tail surfaces up and helps minimize submersion and fouling during landings in either water or tall brush. Additionally, because the tail attachment point is directly located on the fuselage, the mounting is structurally tougher than a T-tail arrangement. As the two V-tail surfaces combine the functions of three traditional surfaces in a traditional configuration (left stab, fin, right stab), the V-tail is lighter and has less wetted area, resulting in parasitic drag reduction. Finally, because both ruddervators are actuated for

either pitch or yaw inputs, there is built-in control redundancy to allow for safe recovery of the vehicle in the event of a single actuator failure.

The tail sizing was chosen to provide adequate stability and damping in both the pitch and yaw axes. Conventional approaches to V-tail sizing have assumed a geometric projection onto the horizontal and vertical planes to compute normal tail volumes as with traditional configurations. While simple, this method fails to account for interference and endplate effects and typically results in undersized tails with correspondingly poor stability behavior of the aircraft. Instead, the equivalent horizontal and vertical tail areas,  $S_h$  and  $S_v$ , are computed using Equation 3-3 (Drela 2000).

$$\begin{aligned} S_h &= S_{Vtail} \cos^2 \theta_t \\ S_v &= S_{Vtail} \sin^2 \theta_t \end{aligned} \tag{3-3}$$

With a V-tail configuration, an additional degree of design flexibility is found in the adjustment of the tail dihedral angle,  $\theta_t$ , adjusting area distributions between vertical and horizontal planes as needed to achieve the desired horizontal and vertical tail volumes,  $V_h$  and  $V_v$ , which are calculated using Equation 3-4.

$$\begin{aligned} V_h &= \frac{l_h S_h}{S_w \bar{c}} \\ V_v &= \frac{l_v S_v}{S_w b} \end{aligned} \tag{3-4}$$

As a result of this sizing, an overall V-tail area,  $S_{Vtail}$  of  $14.5 \text{ dm}^2$  was chosen, with a tail dihedral angle,  $\theta_t$ , of  $35^\circ$  ( $110^\circ$  included angle). These selections result in generous tail volumes, summarized in Table 3-2.

Table 3-2. Nova 2.1 tail design parameters

Tail Span	76.2 cm
Total Area, $S_{Vtail}$	14.5 dm <sup>2</sup>
Tail Dihedral Angle, $\theta_t$	35° (measured from horizontal)
Horizontal Tail Volume, $V_h$	0.38
Vertical Tail Volume, $V_v$	0.029

Developed specifically for low Reynolds number operations, the HT series of tail airfoils was selected to provide excellent performance and low weight. At the root, a 7.5% thick HT14 foil was selected to provide sufficient thickness for structural purposes. This is progressively blended across the span to the 5.0% thick HT12 used at the tip for minimum drag and structural weight reduction. Both foils are unique in their forward positioning of the maximum thickness (HT14 at 18.9%, HT12 at 18.6%), which allows for zero deadband and fully laminar flow, enabling improved control linearity and overall drag reduction. Additionally, the forward maximum thickness position allows for large ruddervator surfaces (40% chord versus 20-25% typical) without structurally weakening the fixed portion of the stabs. These large surfaces enable improved low speed handling, which was an issue with the Nova 2 design. The overall Nova 2.1 tail design is presented in Figure 3-6.

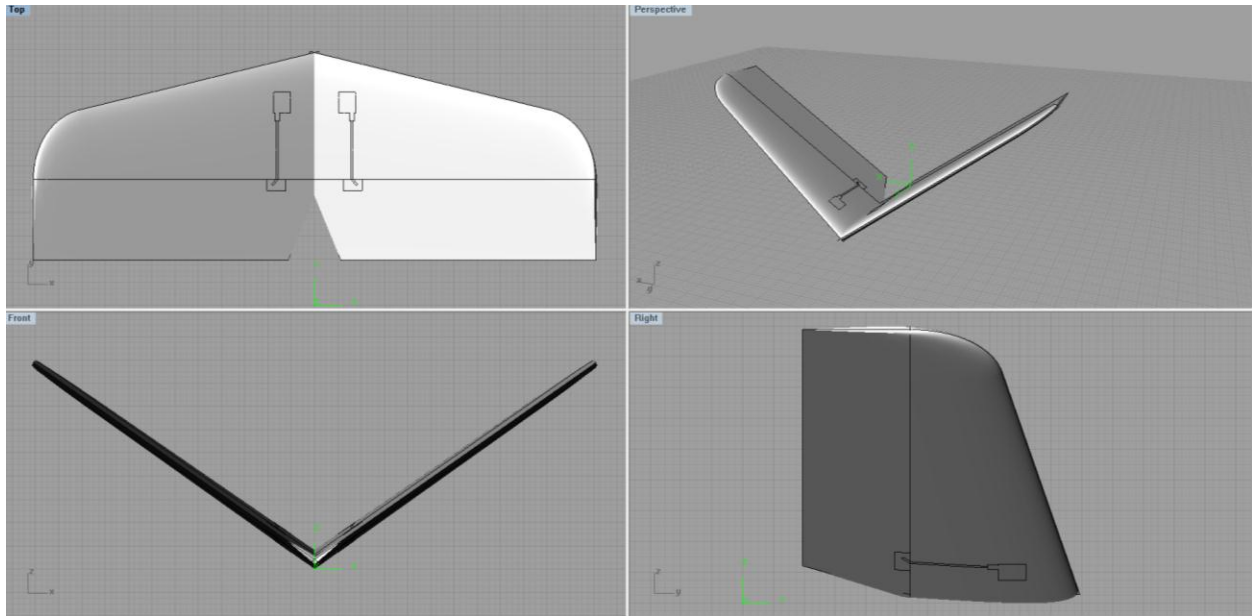


Figure 3-6. Overview of Nova 2.1 tail design.

Finally, to provide minimum drag and optimum control efficiency during all phases of flight, the V-tail height relative to the wing was adjusted to move the tails out of the wing's downwash and fuselage intersection vortices, the results of which are shown in Figure 3-7. Because the wash moves downwards during high-lift phases like takeoff and landing, this adjustment primarily improves cruise efficiency and control effectiveness.

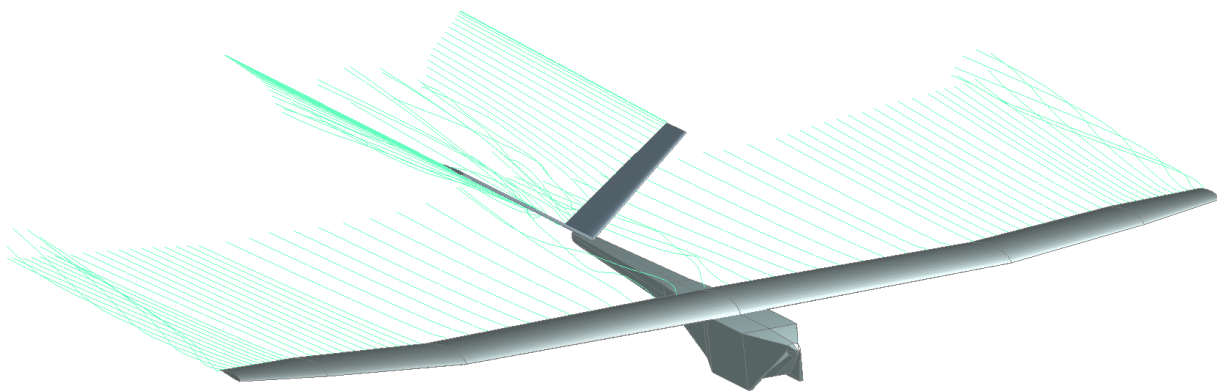


Figure 3-7. XLFR5 streamline analysis illustrating tail placement away from downwash and fuselage junction vortices.

## Fuselage Design and Center of Gravity Considerations

Mirroring the rest of the system, the fuselage design was driven by the payload's data collection requirements. To provide maximum mission flexibility, a readily accessible payload bay 15 cm x 15 cm x 28 cm was chosen to allow deployment of the current payload as well as providing space for optional simultaneous deployment of a second imaging sensor for CIR or other data collection. Initial rough sizing and component placement were performed in Solidworks, with an early configuration model shown in Figure 3-8. To ensure that the CG could be maintained for a variety of mission loadouts, an extended battery tray was included to allow the flight pack to shift fore and aft to compensate for varying payload weights.

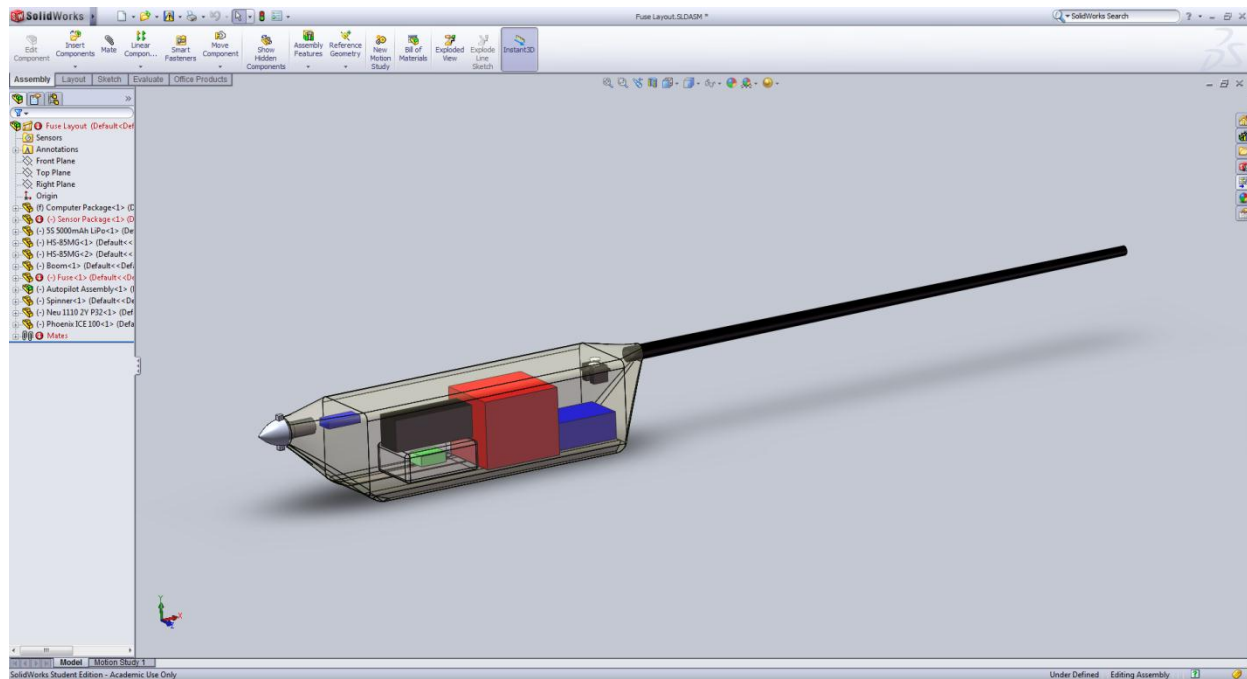


Figure 3-8. Preliminary component placement for CG calculations was completed prior to final fuselage design.

Like previous Nova variants, raised skids were molded on either side of the payload bay to protect the delicate optics from direct impact during operations from unimproved areas. Additionally, care was taken during the final shaping phase to design

in a suitable hand-hold area located at the CG to allow the launcher maximum control over the vehicle during flight operations in high winds. This molded-in relief located below the wing can be seen in the airframe configuration overview presented in Figure 3-9. Because the Nova 2.1 was also to be used as a payload development platform, maximum accessibility was required for rapid reconfiguration. As a result, two large access hatches were incorporated into the top of the vehicle, each compression sealed with thumbscrews during final assembly.

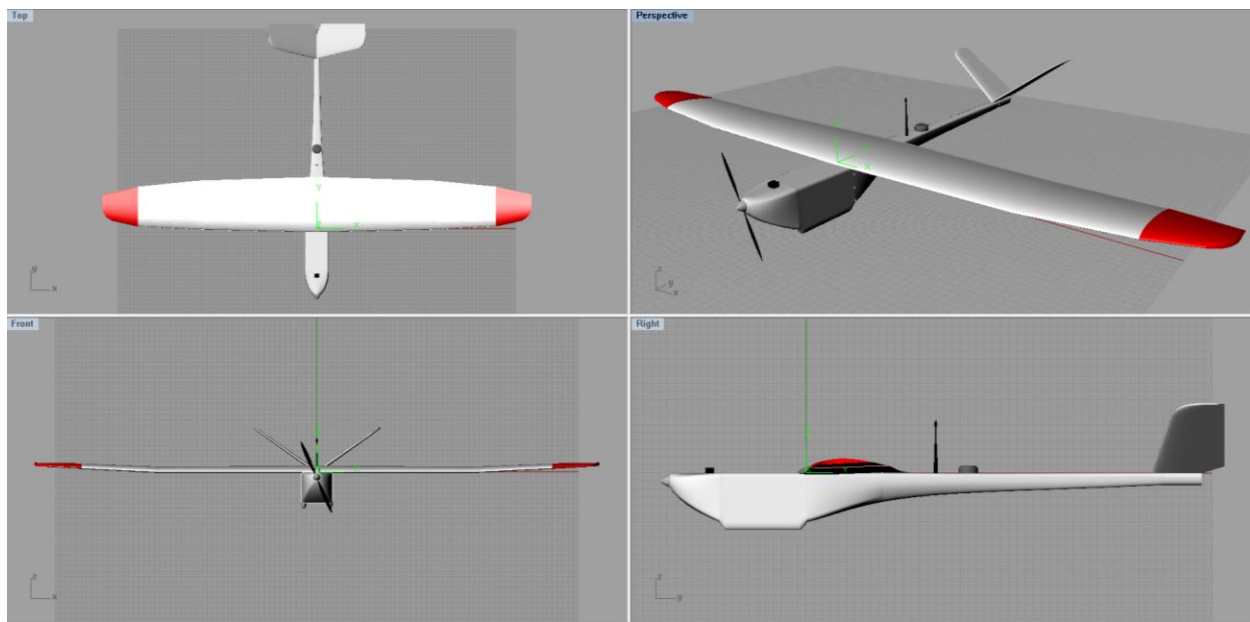


Figure 3-9. Nova 2.1 complete airframe configuration.

To provide adequate static stability along the pitch axis, a static margin of 5% MAC was selected, with the battery placement adjusted for each payload configuration. This static margin is lower than typically found in similar designs in order to minimize the trim drag associated with the nose-heavy condition required by such a configuration. As a result, the airframe's stick-free recovery from pitch disturbances will be weakly stable, implying that although the disturbance will not increase, actual pilot correction may be required to return the aircraft to level flight. Because the Nova 2.1 was designed to be

operated completely autonomously in all phases of flight, a higher degree of pitch stability is unnecessary.

### **Control Redundancy and RDS Linkages**

For roll control, spoilerons were incorporated into the wing at the tip panels, with the option to be raised together as spoilers to provide improved glideslope control for short-field landings. The separate actuators in a spoileron configuration also offer control redundancy in the event of an individual servo failure. Combined with the independently driven ruddervators on the V-tail, this arrangement offers control redundancy on all axes, with two independently wired servos per axis. Because each actuator is wired with its own independent power and signal line, there is further redundancy in the event of wiring failure.

To eliminate the electrical connection across the wing panels normally required for aileron actuation with traditional pushrod controls, a rotary drive system (RDS) linkage was employed. This mechanical servo linkage allows for rapid field assembly, with the angled servo actuating rod sliding into a premolded aileron pocket as the wing panels are joined. This slop-free linkage, shown in Figure 3-10, allows for complete waterproofing of the servos as they are completely contained within the wing center panel and all electrical lines run through the sealed under-wing hatch.

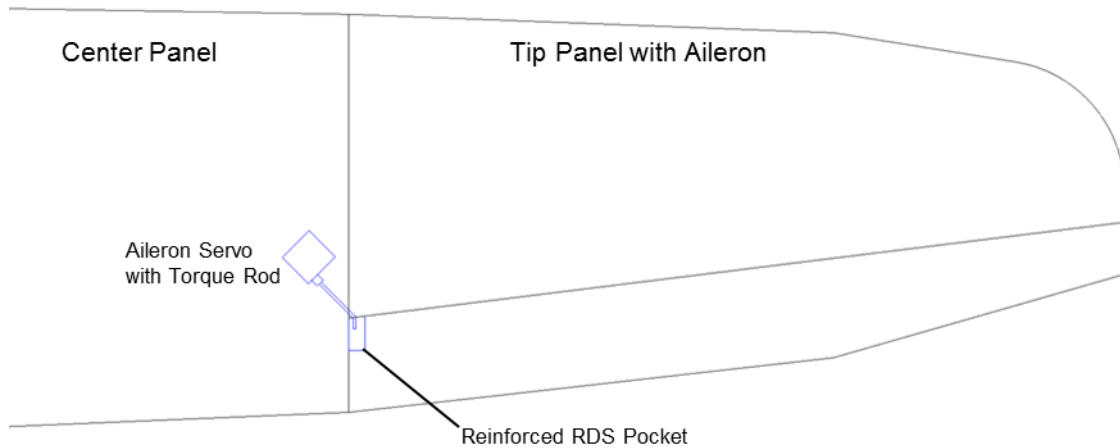


Figure 3-10. Schematic of aileron RDS linkage showing tool- and electrical-free connection.

The V-tail linkages, shown in Figure 3-11, also employ an RDS installation, although in a straight-line configuration which is fixed in place during construction. While more demanding during wing construction and servo installation than traditional pushrod-style linkages, RDS linkages offer improved durability and drag reduction in addition to the previously mentioned waterproofing improvements. As found in work performed on comparably-sized competition RC gliders, the drag from 4 external pushrod linkages was found to be approximately equal to the contribution from the entire horizontal tail (Hepperle 2003), so moving these internally results in definite aerodynamic improvements (Selig, et al. 1996). The improved durability is especially noted because the prototype Nova 2.1 employed standard pushrod linkages, which were frequently damaged during landings in tall grass/low brush. After incorporating RDS linkages, this control surface vulnerability dropped dramatically, with the only recorded linkage damage among three operationally deployed vehicles occurring during a direct impact with a tree upon landing.

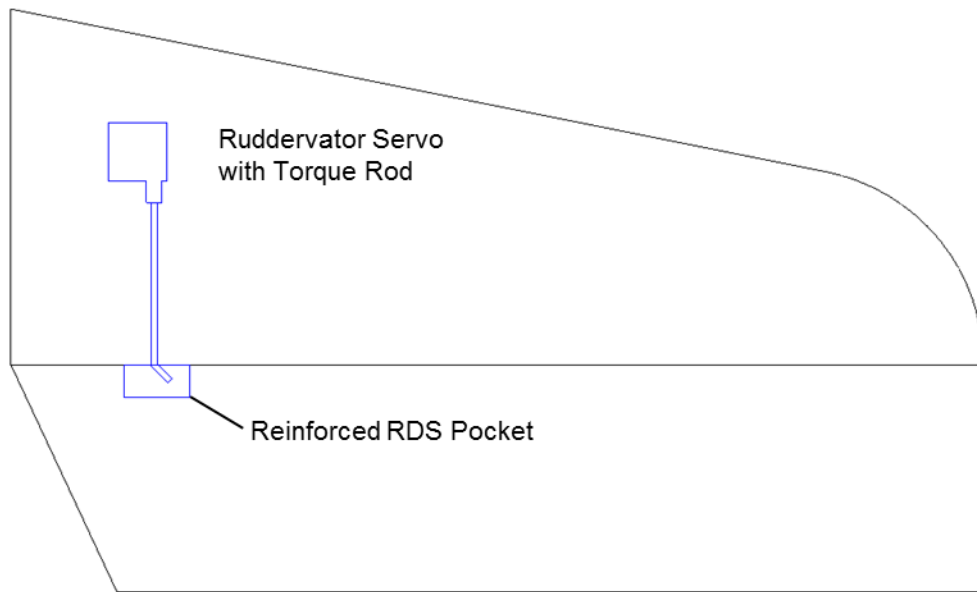


Figure 3-11. Tail RDS linkages.

### Avionics

Based upon lessons learned during previous deployments of the Nova 2 and other amphibious UAS, protection of flight-critical systems from water ingress was highlighted as a key design area (Pisanich and Morris 2002). These systems include the Kestrel™ autopilot hardware and its associated GPS and communications modem, the Electronic Speed Control (ESC) that manages motor operation and regulates power to the actuators, and the actual servo actuators and their associated wiring. To fully protect the Kestrel™ autopilot while maintaining component temperatures within acceptable limits, a finned aluminum enclosure, shown in Figure 3-12, was constructed with IP-67 environmentally rated connectors used to interface with all related hardware.

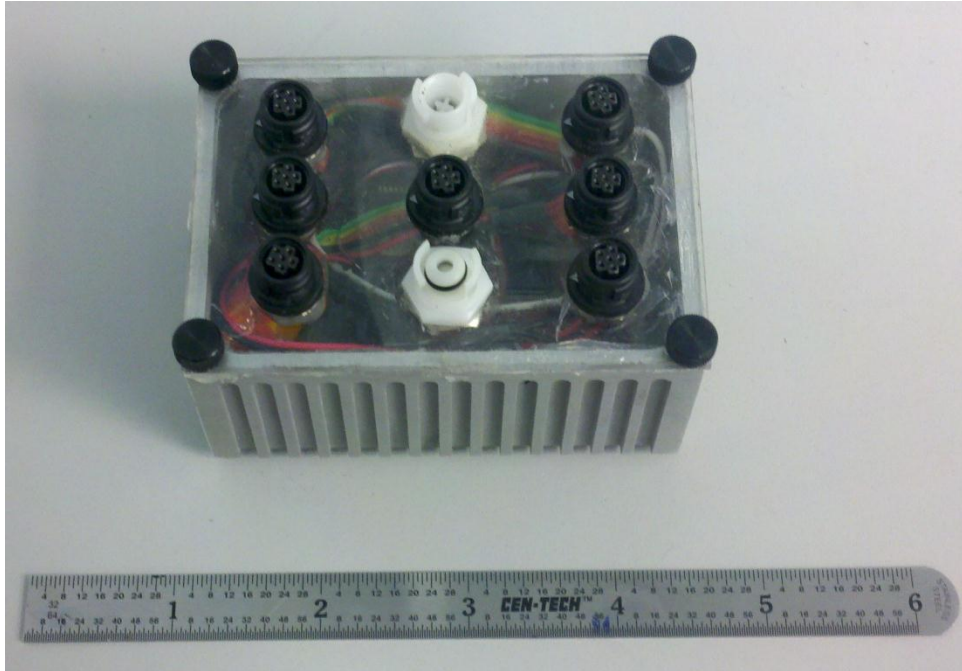


Figure 3-12. Custom machined autopilot enclosure allows for complete waterproofing of critical components while maintaining adequate heat management.

To further protect flight-critical systems, all wiring was environmentally sealed with jacketed cable to eliminate potential shorting hazards. Finally, to minimize water exposure of any flight-critical component, these items were mounted to the inside-top surface of the fuselage, which also aided in cable management efforts. To maintain flexibility as a remote sensing payload development platform, waterproofing for the payload was accomplished with minimal enclosure requirements beyond maintaining the environmental integrity of the fuselage and its hatches. The internal hardware arrangement and hatch locations can be seen in the populated fuselage top seen in Figure 3-13 prior to joining with the bottom fuselage half.



Figure 3-13. Fuselage top populated with electronics prior to joining.

### **Power System and Cooling**

Selection of the power system was motivated primarily by the need to maximize flight duration while minimizing system weight. To maintain hand-launch capability, a power loading of 220 W/kg is required, resulting in a power requirement of 1300W during takeoff and initial climbout. By using a brushless inrunner motor coupled to a sealed planetary gearbox, potential weight savings and efficiency advantages can be gained over comparable outrunner motors with the acceptable downsides of increased cost and periodic gearbox maintenance. The two options are compared below in Table 3-3. Using a three-parameter model, overall motor efficiency can be estimated, with the selected Neu 1509-1.5Y and a comparable Scorpion 4025-12 outrunner (used on the Nova 2) presented in Figure 3-14. At maximum power, the Neu 1509-1.5Y burns 68.9 W less power as waste heat, conserving energy and minimizing cooling requirements.

Additionally, the Neu motor is 77 g lighter than the Scorpion, presenting a 22% weight savings.

Table 3-3. Comparison of motor specifications for Neu 1509-1.5Y and Scorpion 4025-12

	Neu 1509-1.5Y	Scorpion 4025-12
Winding Resistance, $R_m$	0.007 $\Omega$	0.022 $\Omega$
No-load Current, $I_o$	2.00 A	1.80 A
Kv (RPM/V)	358 (geared)	440
Efficiency at 1300 W	94.6%	89.3%
Waste Power at 1300 W	70.2 W	139.1 W
Weight	270 g	347 g

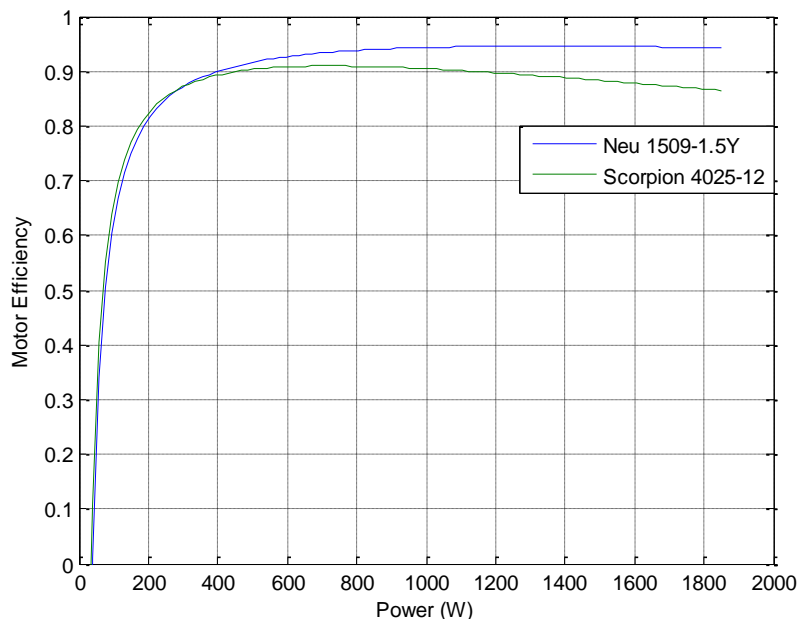


Figure 3-14. Efficiency plots for Neu 1509-1.5Y (inrunner) and Scorpion 4025-12 (outrunner) motor options for 18.5 V input.

The selection of an appropriate propeller is an inexact science, and must balance conflicting requirements for static thrust, cruise efficiency, and motor loading. For static thrust optimization, large diameter, low pitch blades are most effective but limit cruise efficiency. For cruise-phase propeller efficiency calculations, the nondimensional propeller advance ratio,  $J$ , is used, and is given by Equation 3-5:

$$J = \frac{V}{nD}$$

(3-5)

Physically, the advance ratio describes the ratio between the distance the propeller moves through the air during a single revolution, and the diameter of the propeller. For stable cruise flight, peak propeller efficiency occurs when the advance ratio is slightly less (~0.1) than the propeller's pitch to diameter ratio ( $P/D$ ) (Durand 1927). This behavior is shown in Figure 3-15, with maximum overall efficiency increasing for propellers with higher  $P/D$  ratios (coarser pitch).

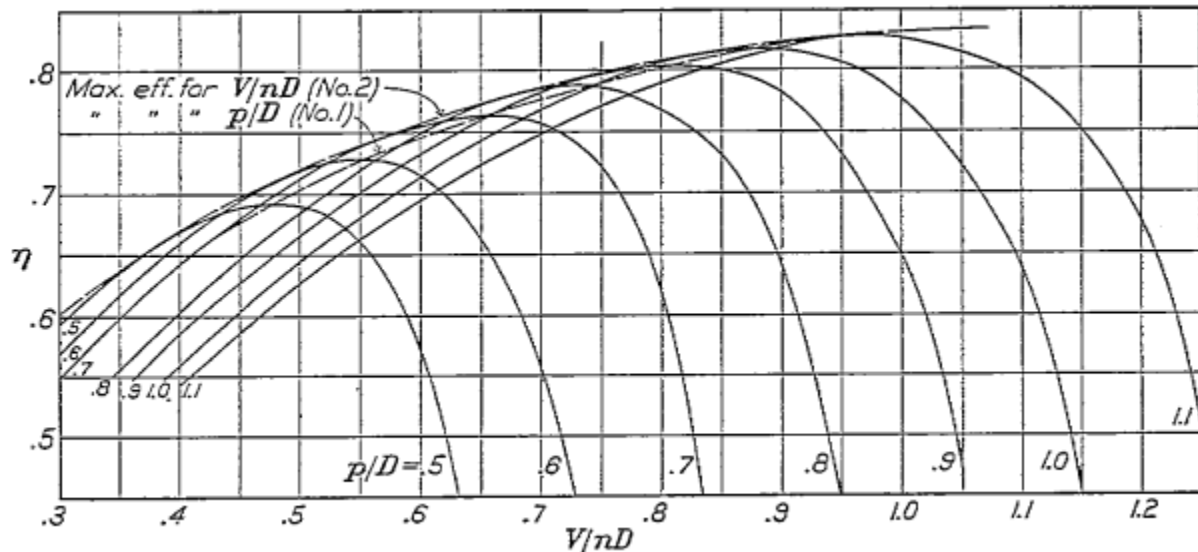


Figure 3-15. Propeller efficiencies for various  $P/D$  and  $J$  ratios. [Adapted from Durand, W. F. 1927. Tests on Thirteen Navy Type Model Propellers. *NACA Technical Report 237* (Page 165, Figure 28).]

Although highly pitched propellers have definite efficiency advantages during cruise, they are frequently stalled when run at full power in a static condition, delivering significantly less thrust. To ensure sufficient static thrust for hand launches while maintaining adequate cruise performance, an Aeronaut CAM 15x13 (385 mm diameter, 330 mm pitch,  $P/D = 0.857$ ) folding propeller was selected. This propeller adequately

loads the selected motor to the desired input power levels and offers an operational benefit of folding back during landing to minimize potential blade damage.

To power this motor/propeller combination, a Phoenix Ice 100 ESC was selected, offering onboard data logging and an onboard switching regulator to efficiently power the plane's servo power bus. The main system battery, an 18.5 V 11 Ah rechargeable lithium polymer pack from MaxAmps, was carried over from the Nova 2 system, as it offered superior energy density and satisfied design duration requirements.

Due to the unique waterproofing requirements of the system, cooling of the main heat sources in the propulsion system, the motor and the ESC, required slight departures from typical mounting procedures. Able to be safely submerged, the motor was mounted in front of a waterproof firewall, and was exposed to external cooling air through vents in the nose of the fuselage. Additional cooling was provided by the motor's finned exterior and internal fan. To protect the ESC from water while providing ample cooling, an external heat sink was flush-mounted to the fuselage exterior, and the ESC was bonded to this with thermally conductive epoxy. The overall configuration of the power system is shown in Figure 3-16. This cooling strategy proved extremely effective, with all propulsion components operating just above ambient temperatures, even during flight tests in 35° C ambient conditions.



Figure 3-16. Nova 2.1 propulsion system, with Aeronaut CAM 15x13 folding propeller, externally vented Neu 1509-1.5Y, and Phoenix Ice 100 external heat sink.

### **Fabrication and Assembly**

To minimize weight and provide maximum RF transparency, the fuselage of the Nova 2.1 was constructed using a hybrid layup of fiberglass and aramid fabrics with epoxy resin. After prepainting the fuselage female molds, a cosmetic layer of 70 gsm bidirectional E-glass was first laid up, followed by two layers of 170 gsm bidirectional aramid fabric. A 4-harness weave was used to help the aramid fabric conform to the fuselage curves without excessive relief cuts. Local unidirectional carbon fiber reinforcements, shown in Figure 3-17, were placed around the wing mount and hatch locations to provide adequate strength without excessive weight or RF blocking. This layup was then vacuum-bagged to remove excess resin and post-cured for 8 hours at 50° C for increased stiffness. By using aramid fabric for the fuselage, a light and tough structure could be created, with excellent damage tolerance. Unlike carbon, which shatters upon impact, aramid composites tend to locally wrinkle without tearing, keeping

damaged sections together. This enables rapid field-repairs, increasing operational availability.

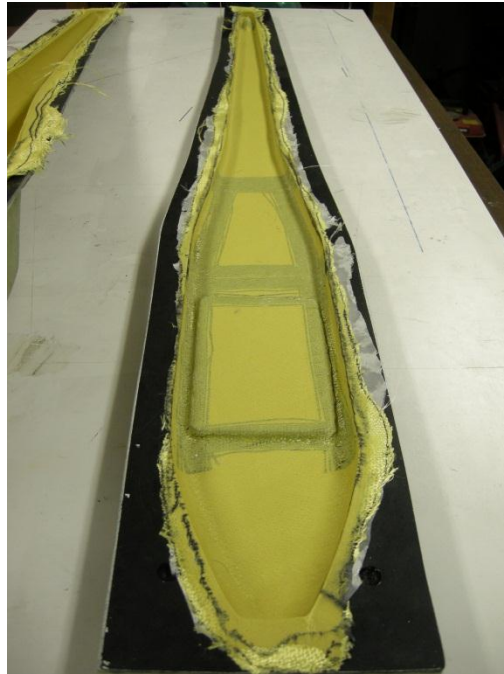


Figure 3-17. Local unidirectional carbon reinforcements around wing mounts and hatch locations.

To guarantee a strong, watertight seal without wet seaming, a seam “joggle” was molded into the fuselage top, depicted in Figure 3-18 (Drela 2003). This joggle offsets the overlapping fabric at the part seam to allow consistent overlap for strength and to minimize the weight of any required adhesive for secondary bonding of the fuselage halves.

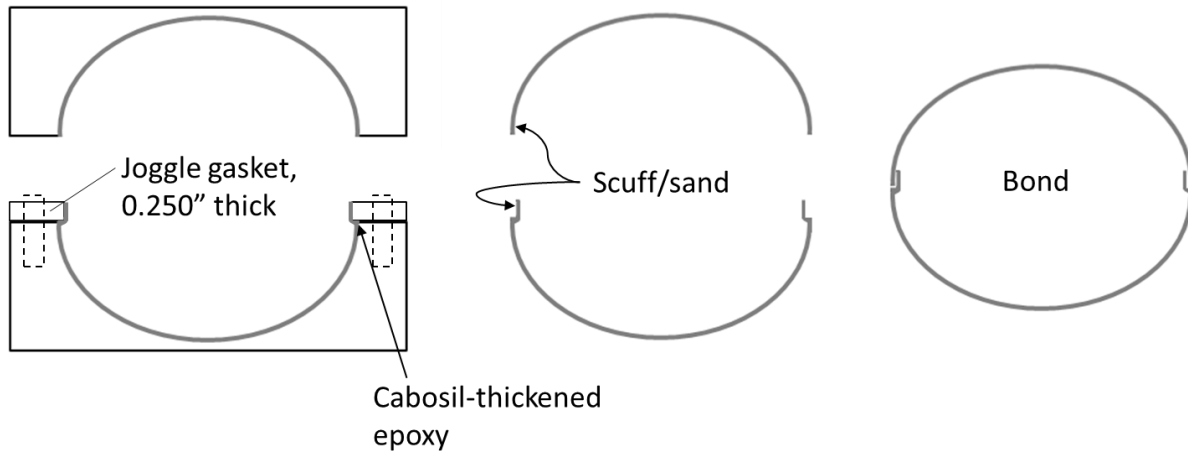


Figure 3-18. Schematic of fuselage halves built with molded-in seam “joggle”.

After curing, the completed fuselage halves were trimmed and demolded in preparation for avionics installation into the fuselage top. Because the parts were painted in the mold, the epoxy resin bonds chemically and mechanically to the paint, leaving a tough exterior surface with no further finish work required.



Figure 3-19. Completed fuselage prior to avionics install in preparation for joining.

The wings and tails were constructed using CNC-hotwired foam cores with precut slots for joiner tubes, pitot lines, and actuator wiring. These cores were joined into center and tip panels, with reinforcements added for RDS pockets, wing bolts, and other mounting hardware, then finish sanded in preparation for bagging. Strips of adhesive-backed bias-cut aramid fabric were then applied for leading edge reinforcement and to serve as skin hinges. The actual wing skins, 54 gsm E-glass with 160 gsm unidirectional carbon reinforcements, were then laid up onto prepainted mylar carriers, as shown in Figure 3-20. These carriers were then placed over the cores and vacuum-bagged to ensure adequate bonding. Like the fuselage, the wings and tails were postcured for 8 hours at 50°C.

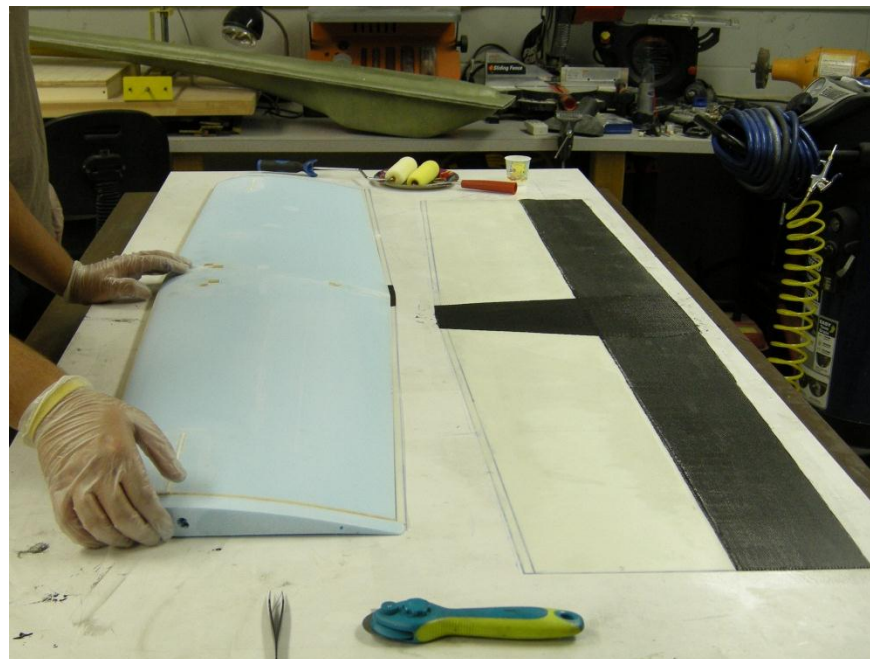


Figure 3-20. Wing construction picture showing selective local reinforcement with unidirectional and bidirectional carbon fabrics.

### **Performance Evaluation**

Overall, the Nova 2.1 demonstrated significant performance gains over its predecessor. In its production form, the Nova 2.1 deployed an identical payload to the

Nova 2, but with a 16% lower flying weight, despite having added 21% more wing area. The resulting reduction in wing loading, summarized in Table 3-4, led to dramatic improvements in flying characteristics, especially noted in the relative ease of hand-launching due to the lower stall speed. Additionally, overall flight stability and rapid wings-level correction following gust perturbations was noted, improving data collection and allowing for less conservative sidelap values and higher ground coverage efficiency.

Table 3-4. Comparison of as-built Nova 2 and Nova 2.1 platforms

	Nova 2	Nova 2.1
Wingspan, $b$	2.44 m	2.74 m
Wing Area, $S$	67.4 dm <sup>2</sup>	81.6 dm <sup>2</sup>
Typical Weight, $W_{typ}$	6.1 kg	5.1 kg
Wing Loading, $W/S$	9.05 kg/m <sup>2</sup>	6.25 kg/m <sup>2</sup>
Cubic Wing Loading, $W/(S^{3/2})$	11.0 kg/m <sup>3</sup>	6.92 kg/m <sup>3</sup>

Relative to its predecessor, the Nova 2.1 also proved to be a much cleaner aircraft, with a significantly smaller frontal area as a result of the tractor configuration. Although this has obvious benefits for cruise efficiency, it also meant that landing approaches were very long and shallow. From a final breakout altitude of 40 m, dead-stick autoland approaches often took 450 m to complete. Although manual landings could be somewhat shortened, this presented a potential problem for operations from many forested areas which motivated work to integrate flaps onto later aircraft.



Figure 3-21. Disassembled Nova 2.1 illustrating small deployment volume.



Figure 3-22. Assembled Nova 2.1 aircraft.

## CHAPTER 4 SYSTEM DEPLOYMENT AND EVALUATION

### ISR Mission Profile

For typical ISR deployments, long the mainstay of sUAS applications, the operational objective is straightforward: provide persistent visual intelligence over selected targets of interest. The level of mission planning necessary to achieve this objective is minimal and simply requires designation of GPS waypoints for each reconnaissance target while selecting adequate takeoff and recovery areas. As shown in the sample flight profile in Figure 4-1, mission execution typically begins with a climb to a cruise altitude (typically constrained by the resolution of the video sensors), followed by a cruise to the selected target area. To provide maximum duration for deployment of the selected sensor package, all flight is normally conducted at the minimum power airspeed,  $V_{mp}$ . Upon reaching the designated target waypoint, the sUAS will enter a continuous loiter about the target, providing constant visual intelligence until an alternate target is selected or available endurance is exhausted. At that point, the sUAS then returns to the selected recovery area at  $V_{mp}$  before descending and executing its final recovery flight path (traditional, deep stall, parachute, etc.).

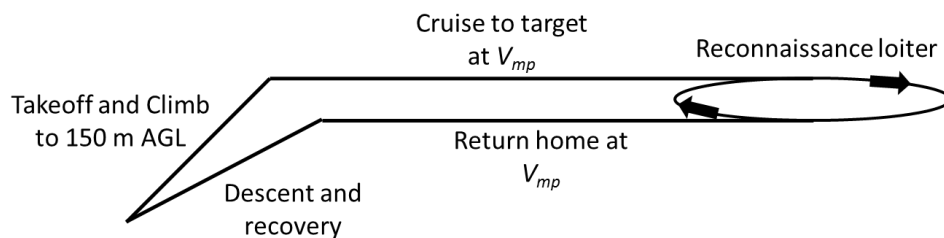


Figure 4-1. Typical sUAS flight profile for ISR missions.

Because the overall flight path is relatively simple, there is little room for flight planning optimization beyond logical ordering of selected targets, either by flight distance or target priority. Additionally, because overall flight optimization focuses on keeping the sUAS' optical sensors over the target as long as possible, endurance maximization becomes a key objective. As a result, unless mission circumstances dictate otherwise (e.g. brief dashes between priority targets or convoy tracking), all cruise and loiter flight phases are conducted at  $V_{mp}$  to conserve power. This fixed operating condition also simplifies vehicle design, as all aerodynamic and propulsion optimization can be centered on maximizing performance in a narrow airspeed window.

### **Photogrammetry Mission Profile**

Conversely, for aerial photogrammetry missions, flight paths are often highly complicated in order to satisfy coverage requirements. In comparison to the handful of target locations needed for a typical sUAS ISR mission, average photogrammetry flights for the Nova 2.1 system require over 60 waypoints to establish accurate flight lines that satisfy data collection specifications and maintain designated image overlap. Depending on desired output resolution and the resultant flight altitude, optimal cruise speed may vary; it may be beneficial to fly as slow as possible to guarantee sufficient overlap for low-altitude, high-resolution missions or to fly quickly in an effort to minimize redundant data collection on high-altitude, low-resolution flights. This broad operational speed range, coupled with the operational requirement for a low stall speed to maintain hand-launchability, presents a significant design challenge for vehicle and propulsion optimization.

## **Flight Planning Implications**

For sUAS-based remote sensing applications, flight planning is an essential part of overall flight optimization. Although on-site and on-demand planning is important, the most efficient deployments are achieved with as much advanced preparation as possible. Flight plans must take into account environmental variables like wind speed and direction, and mission parameters like the orientation of the target area and desired output resolution. Finally, to improve operational efficiency, efforts should be made during the flight planning stages to maximize the payload's time on target by minimizing mission overhead, which includes takeoff and landing flight phases as well as any turns made at the ends of flight lines. A systematic approach to flight planning has been developed by the UF UASRG to ensure a semi-optimum data collection for any situation, concluding in a flight plan that can be further optimized by speed-to-fly theory.

Regulatory restrictions are a key factor in mission management and are the first real planning consideration following an overall feasibility analysis. With some limitations around restricted areas, sUAS operation is possible in most classes of airspace on a case-by-case basis. However, as a general rule, flight should be limited to Class G airspace. Because the typical 200 m flight altitude for the Nova payload exceeds the 400 ft (122 m) AGL limit for sUAS imposed by the Federal Aviation Administration (FAA), a licensed manned pilot is required to serve as Pilot-in-Command of the system. Although somewhat cumbersome, this requirement has the benefit of allowing the sUAS to bypass the restriction of flight closer than 5 miles (8 km) from any airport, significantly expanding available deployment areas. Additional airspace access is gained by fitting an optional altitude-encoding transponder, which allows the Nova 2.1 system access inside the 30 nautical mile (56 km) veil of many larger airports around

the country. With these two capabilities, the Nova 2.1 sUAS has achieved unprecedented access to the majority of Class G airspace throughout the country, with the UF UASRG spearheading regulatory acceptance of sUAS research deployments.

The next step in the mission optimization process is dependent on final image quality parameters. The output resolution (typically a specified ground sample distance) desired for final data deliverables is first used to select an appropriate flight altitude for the vehicle. Dependent on the desire for 2D or 3D photogrammetric processing, the required sidelap percentage is then calculated, either directly or using a chart like in Figure 1-2, to determine the side airbase and adjacent flight line spacing. Once these flight parameters are set, the actual generation of flight lines is delegated to the Ground Control Station (GCS) and the flight planning software. Although the software automatically generates the precise waypoints, the operator retains overall control of the process, both for regulatory compliance and operational efficiency. At this stage, the preliminary flight plan consists of all necessary flight lines extending to the FAA-imposed 1 mile (1.6 km) VLOS limit, and the flight lines can be translated and rotated as a whole onto any target area.

The next factor to be considered in the mission planning process is target area geometry. Flight paths for optimal data collection are highly dependent on target-specific geometry and may result in significantly different planning strategies, as shown in Figures 4-2 and 4-3 for broad-area and linear targets. While areal targets frequently permit rotation of the flight lines to minimize crab angle, target areas with excessively high aspect ratios (linear features like pipelines and levees) will force the flight lines to be parallel to the longer transect regardless of wind direction. This is to minimize the

number of turns during which data collection is not ongoing. Additional geometric constraints may arise from nearby obstacles or regulatory restrictions that prohibit flight over regions directly adjacent to the target area, necessitating flight parallel to the prohibited area to prevent over-flight during turnaround maneuvers.

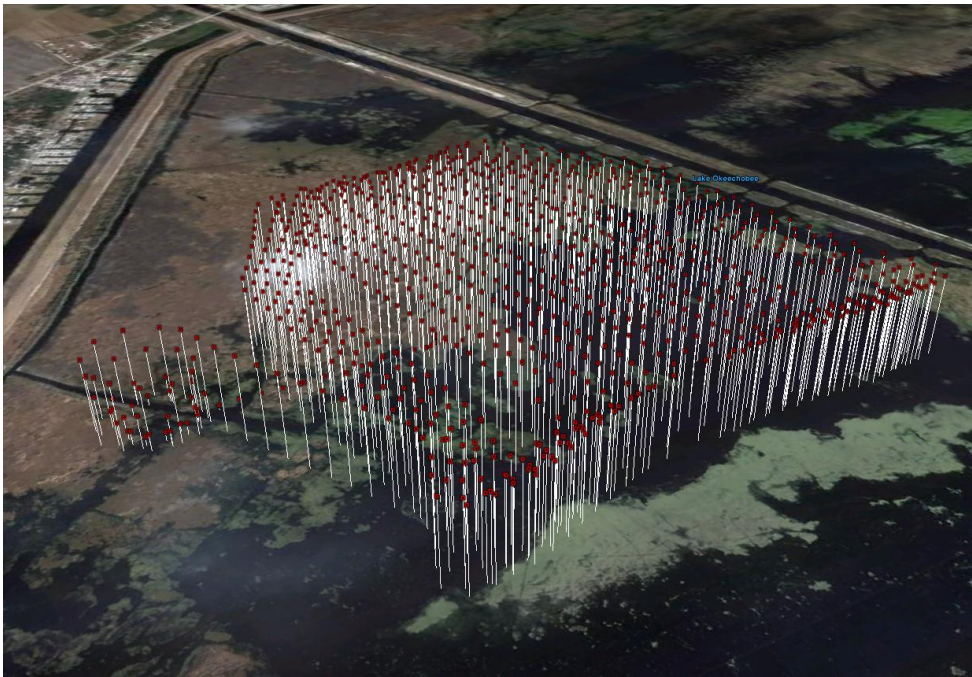


Figure 4-2. Dipole flight path over areal target on Lake Okeechobee, FL with each point representing a single image exposure.



Figure 4-3. Linear flight path over levee target with takeoff and landing spirals visible.

For all other areas without over-flight or aspect ratio restrictions, wind direction is the predominant geometric consideration and flight lines can be oriented in any direction. The most efficient way to process aerial mapping data for mosaicking is with images that are orthogonal to each other, maximizing image overlap and minimizing redundant data storage. The 'strapdown' configuration of the Nova payload dictates that it is most efficient for the flight lines to be oriented with the wind so the sensor orientation aligns with the ground track instead of 'crabbing' as a result of crosswind. This ensures that the full width of each orthogonal image is available for overlapping coverage

At this point, the flight plan consists of a set of parallel flight lines that will guarantee sufficient photogrammetric coverage in an improved layout with geographic and geometric constraints. The final piece of flight planning and optimization is to set turns and properly order flight lines. At normal cruise speeds and with a conservative

maximum bank angle of  $35^\circ$ , the Nova 2.1 has a minimum turning radius of about 75 meters. This simple performance measure is by far the most influential in determining optimal flight line sequencing. In an ideal flight plan, all end-of-line turns finish with the UAV established in a wings-level position, aligned with the next flight line, immediately prior to entering the mapping target area. This ensures that coverage isn't dropped at the area boundaries and eliminates excessive collection of non-target data. To accomplish this, a variety of flight patterns are available, with the most common dipole and parallel-track options shown in Figure 4-4. If the flight line spacing combined with downwind drift is less than the specified minimum turn radius, then the dipole flight pattern takes priority, allowing the UAV to skip one or more adjacent flight lines, sacrificing the additional flight distance during the turnaround to prevent the UAV from overshooting its desired path. If the combined spacing is greater than the turn radius of the aircraft, then the parallel-track flight path, a common pattern for aerial searches, takes priority (Santamaria, et al. 2008). The most efficient option due to its short turnarounds, the parallel-track flight pattern is the preferred arrangement, and is used for most flights unless very low altitudes (and thus, small flight line spacing) are required. In actual implementation, the flight planning software will take the forecasted wind direction and magnitude into account and project the additive/deleterious effects on the turn radius. The flight management algorithm then takes the required array of flight lines from the preliminary flight plan and orders them as called for by the specified flight pattern.

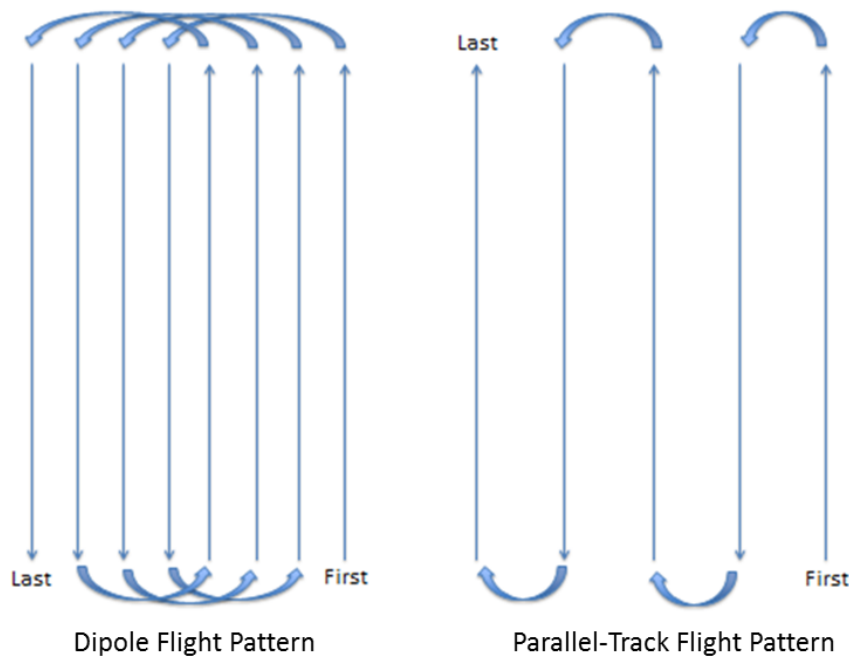


Figure 4-4. Flight line patterns for remote sensing applications.

On site, if the flight team determines that the wind has diverged significantly from the forecasted direction or magnitude, then a strategy is put in place for in-flight assignment of the flight plan. Once launched, the aircraft will enter a circular orbit about a preselected takeoff point. After making a complete orbit, the autopilot is then able to accurately estimate wind direction and magnitude. At this point, updated parameters can be automatically fed into the flight planning software and a new flight plan, properly oriented into the wind, can be uploaded instantaneously. Finally, because the autopilot continuously updates its estimations of the winds aloft, any significant changes in conditions can be easily dealt with by uploading a new automatically generated flight plan, saving significant time and effort over manual adjustment by the ground station operator. Regardless of any in-flight wind direction change, the final step to flight optimization occurs once airborne. The speed-to-fly theory explained in later sections sets the desired airspeed for each upwind and downwind flight line for maximum

efficiency. The overall flow for flight plan development is summarized below in Figure 4-5, with relevant parameters indicated for each design stage.

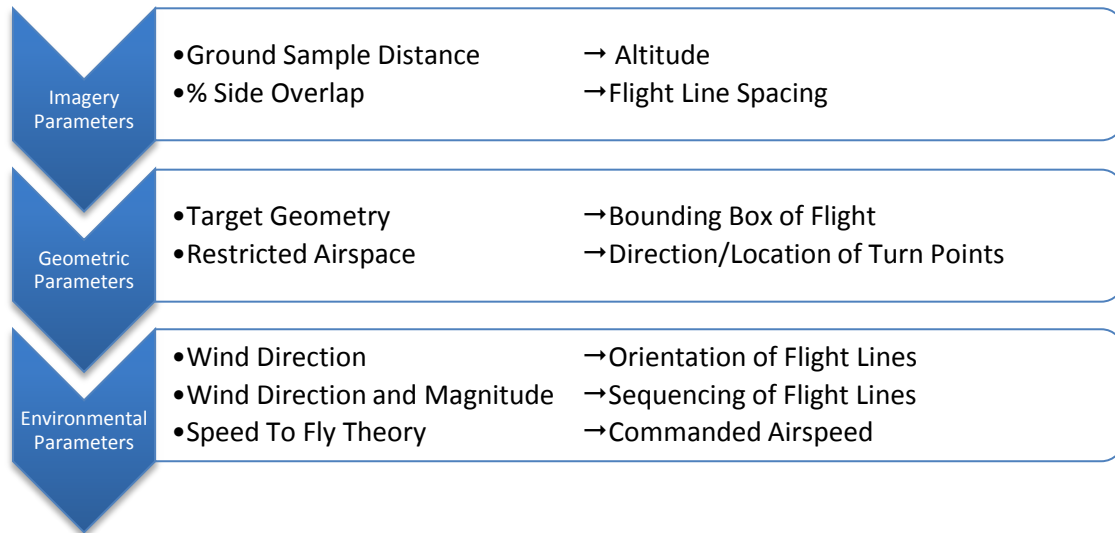


Figure 4-5. Flight plan design procedure and relevant parameters.

### Flight Planning Optimization

In addition to ensuring sufficient photogrammetric coverage through appropriate arrangement and ordering of flight lines, significant operational efficiency gains can be made by minimizing mission overhead. Loosely defined as any flight time not spent collecting data over the target area, mission overhead includes takeoff, climb, descent, and landing phases, transit between the target area and the launch/recovery site, and any orienting turns required to align the UAV with its target flight lines. Without active effort to minimize overhead, it can easily exceed 50% of overall flight time. Even after months of system deployment, non-optimal paths like that shown in Figure 4-6 were used, highlighting the gains still to be made by minimizing mission overhead.

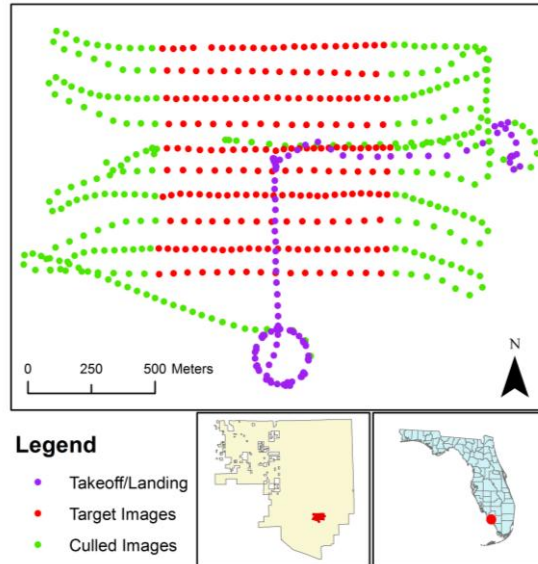


Figure 4-6. Parallel-track flight plan for mapping road degradation in Picayune Strand State Forest, FL.

To fully optimize total mission overhead, power consumption during all flight phases must be addressed. A normal flight profile for autonomous aerial mapping flights, shown in Figure 4-7, has significant room for improvements to reduce overall time and power consumption. For takeoff and initial climb-out phases, best climb speeds should be used instead of more typical full throttle maneuvers in order to minimize the total energy expended getting to cruise altitude. Additionally, while the initial takeoff heading is determined first by local site factors (power lines, trees, roads) and then by wind direction, the traditional spiraling climb to altitude should be supplanted by a direct ascending route to the first flight line, minimizing the time and power needed to transition to the data collection portion of the flight.

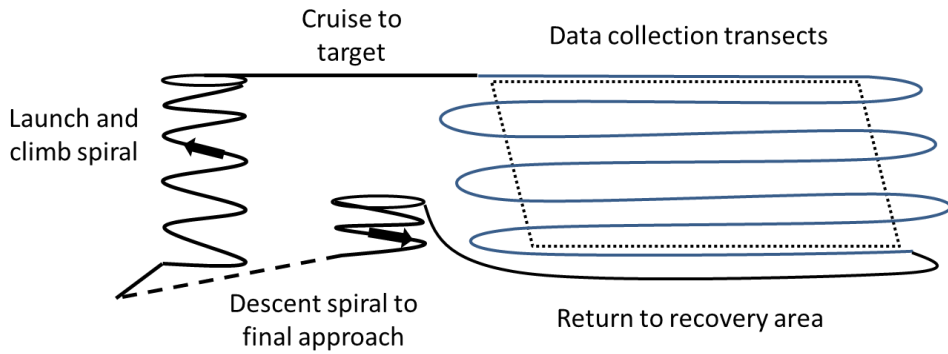


Figure 4-7. Flight profile for a typical sUAS-based aerial mapping mission.

As discussed previously, routing of turns between subsequent flight lines was initially done by hand, and excessive margin was left at the ends of the area boundaries to guarantee adequate alignment of the payload prior to entering the target area, as shown in Figure 4-6. By more aggressively routing necessary turnaround maneuvers, the automated flight planning software will minimize mission overhead while maintaining necessary overlap parameters.

During mapping projects over large continuous areas where multiple flights are needed, it is not possible to readily calculate the exact number of complete transects available per flight due to various environmental uncertainties. As a result, it becomes important to accurately estimate remaining battery capacity throughout the flight in order to maximize available coverage while preventing over-discharge of expensive system batteries. If sufficient capacity is available to completely cover the given target area, however, the mission should be flown as fast as possible (while maintaining endlap minimums) in order to maximize the number of possible flights per crew, per day.

One final note for overall mission efficiency regards the final descent and landing phases of flight. Instead of returning to the recovery area at the data collection altitude, burning precious energy that could have added additional transects, the initial descent

should begin as the UAV completes its final flight line, allowing a power-off glide to the landing area. While not practical in areas where minimum altitudes must be maintained to clear obstacles or terrain, this final optimization provides an additional target for improving total flight efficiency. A more direct, optimized mission profile is shown in Figure 4-8, demonstrating the gains possible through the elimination of mission overhead.

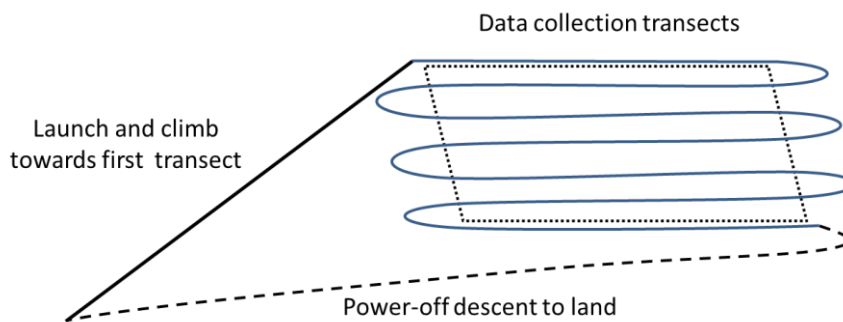


Figure 4-8. Optimized flight profile with more aggressive takeoff/climb routing and a power-off descent to landing.

### **Operational Feasibility of sUAS for Remote Sensing Applications**

While 1 hour flights covering 500 m × 500 m target areas are acceptable for preliminary research applications, true operational feasibility of battery-powered sUAS for remote sensing applications will require, at a minimum, full coverage of 2 km × 2 km targets. This will maximize areal coverage within current FAA-mandated 1 mile (1.6 km) VLOS restrictions, and provide operators with the ability to map 1000 acres (400 ha) of terrain per flight, dramatically increasing the sUAS' operational value as a scientific tool. Although this endurance level is certainly achievable for sUAS with current battery technologies, a design challenge is brought on by a mapping payload's higher than average weight and the desire to maintain hand-launch capability. Because the scope of typical system deployments often exceed single flight coverage, with multi-day missions

common, minimization of the required time for each flight is critical to increase flight crew effectiveness. In addition to actual flying time required for each mission, significant ground intervals may be required for system mobilization to new target areas, excluding a normal 10 minute airframe turnaround. As a result, both mission planning and airframe optimization should focus on maximizing coverage efficiency with respect to both time and power requirements. Ultimately, this leads toward a need to widen the available speed range of the sUAS to provide a high optimal cruise speed for rapid coverage while maintaining operational flexibility with a sufficiently low stall speed to permit hand-launching.

## CHAPTER 5 SPEED TO FLY APPLICATION

### **Theory**

Because hand-launched sUAS tend to have lower cruise airspeeds (15-20 m/s), wind conditions play a large role in determining their ultimate ground coverage. Additional endurance constraints arising from current electric propulsion systems mean that unlike traditional wet-fueled platforms, operators cannot simply fuel up more and fly longer in significant wind conditions. Taking into account heavier optical payloads associated with aerial mapping applications, little margin remains for additional battery weight. As a result, a novel flight planning strategy is needed to aid in path optimization for remote sensing missions. For parallel-track flight plans, with flight paths always being flown directly into or with the wind, the wind interaction is simplified to a purely additive or subtractive term for ground coverage. Neglecting turns, altitude changes, and small disturbances, this further simplifies the optimization problem to total ground coverage with vehicle speed and wind speed as the only variables.

With the ultimate goal being to reduce overall energy expenditure per linear kilometer flown in order to yield the highest number of mapping transects (defined as one pair of upwind and downwind legs across the target area), an analogous approach was found in another branch of aviation familiar with limited power sources: cross-country soaring. Without a direct motive source, glider performance is extremely sensitive to energy management. For cross-country gliding flights, maximizing distance traveled with the potential energy (altitude) gained by climbing in thermal updrafts is a primary concern and this optimization is dramatically affected by prevailing winds. As a result, glider pilots use a speed polar to determine the optimum speed-to-fly (STF) in

headwind or tailwind conditions (Federal Aviation Administration 2007). In a similar fashion, the power curve of a powered aircraft can also be used to calculate optimum range airspeeds in variable wind conditions (Phillips 2004).

To perform this analysis, a sample Nova 2.1 power curve, presented in Figure 5-1, was generated using XFLR5-generated drag estimates and assuming 100% propulsion efficiency for simplicity. Immediate visual analysis of this sample curve presents two important data points. The first is the minimum power consumption airspeed,  $V_{mp}$ , ( $mp$  = minimum power), which is the commanded airspeed to be maintained in order to maximize level flight duration. This airspeed remains constant independent of wind conditions and requires a minimum input power level,  $P_{min}$ , to be maintained. This is the optimum cruise airspeed for zero wind conditions and is typically maintained during most sUAS missions, especially for ISR applications. The second, less obvious value is the point at which a tangent line drawn from the origin intersects the power curve. This line represents the minimum energy consumption per unit distance, which is given by the slope of the tangent line ( $= P/V$  [J/m or Wh/km]). For convenience, this value will be termed the Distance Specific Energy Consumption (DSEC). The abscissa at the point of intersection corresponds to the airspeed value termed  $V_{mr}$  ( $mr$  = maximum range), which yields the optimal range. To maintain this airspeed, an optimal input power value of  $P_{mr}$  is required. In still air conditions, where the airspeed and groundspeed are equal, such analysis holds true. In headwind or tailwind conditions, however, the calculations proceed slightly differently.

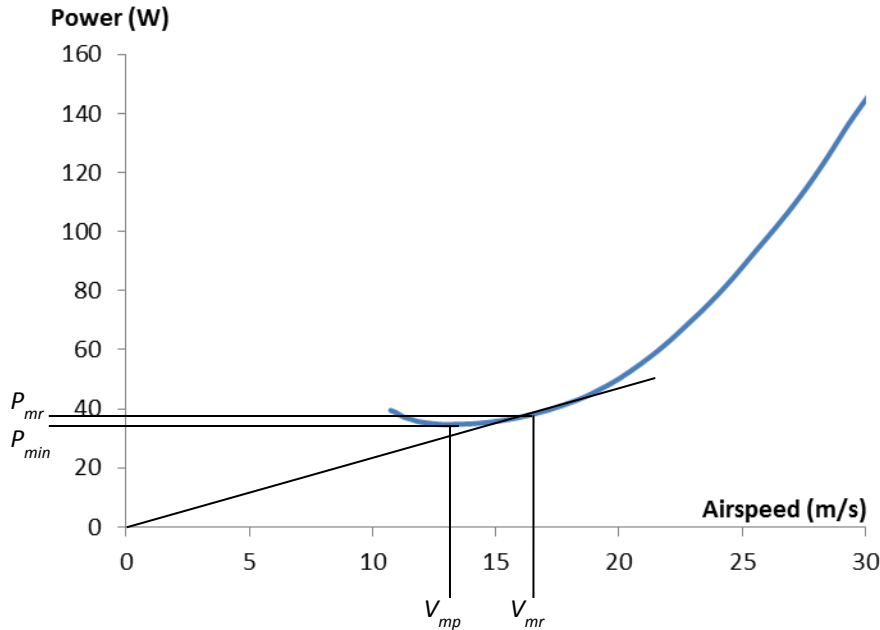


Figure 5-1. XFLR5-generated power curve (assuming 100% propulsion efficiency) for Nova 2.1 illustrating graphical computation of optimal STF in still air. By flying at  $V_{mp}$  ( $mp$  = minimum power), power consumption is held at a minimum and maximum duration is achieved. However, flying at  $V_{mr}$  ( $mr$  = maximum range), minimizes the Distance Specific Energy Consumption (given by the quotient  $P/V$ ) and maximizes the distance traveled per unit of input energy.

In pure headwind/tailwind conditions, the effective groundspeed is found through a simple additive relationship with the airspeed and wind speed, with headwinds reducing effective groundspeed. Graphically, this results in a positive shift of the tangent line along the x-axis, corresponding to the magnitude of the headwind, as seen in Figure 5-2. To compute  $V_{mr}$  corresponding to a 10 m/s headwind (typically the highest wind speed to permit safe operation), the x-intercept is shifted 10 m/s right and a new tangent line with the power curve is found. This line's higher slope indicates that the headwind has had a negative effect on efficiency, increasing the DSEC according to Equation 5-1:

$$DSEC = \frac{P}{V \pm V_{wind}}$$

(5-1)

Additionally, the new  $V_{mr}$  value is found to be higher than the original still air figure,  $V_{mr}^*$ , indicating a need to accelerate into a headwind for increased ground coverage efficiency.

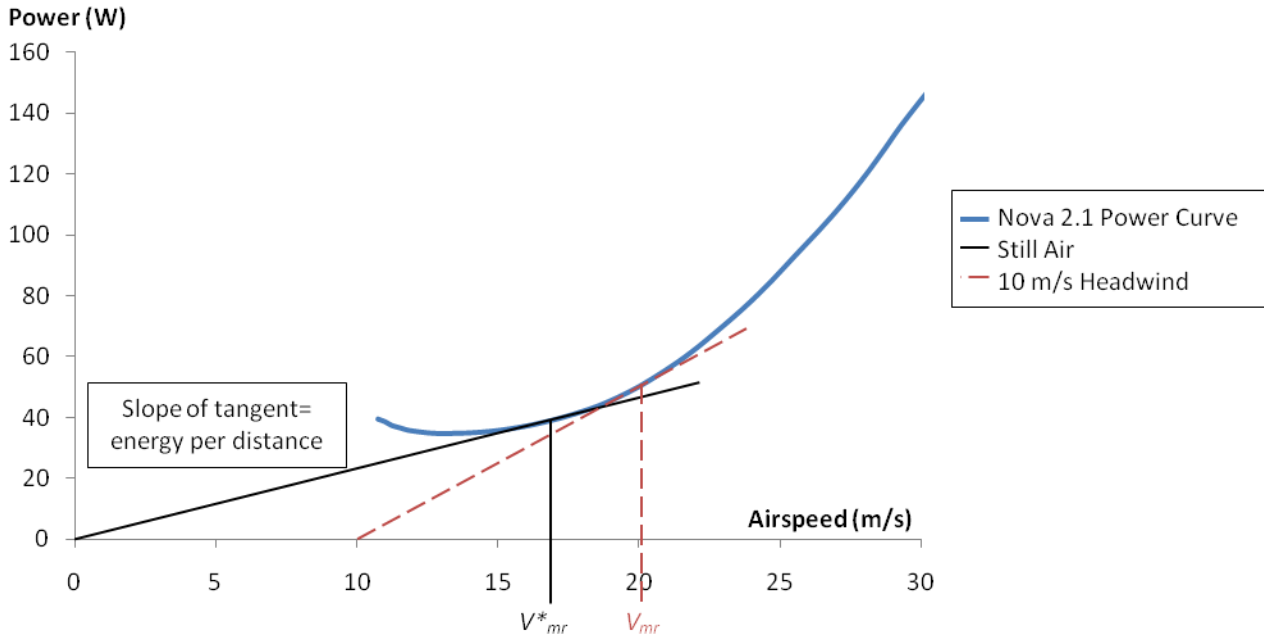


Figure 5-2. XFLR5-generated Nova 2.1 power curve illustrating application of STF theory. With a 10 m/s headwind, the tangent line's x-intercept shifts to the right indicating a loss in effective groundspeed and the new optimal airspeed,  $V_{mr}$ , is found to be higher than the still air value,  $V_{mr}^*$ .

Although increasing the commanded airspeed on upwind passes does increase the immediate energy consumption rate, the overall energy expenditure for the flight line is lower if flown at  $V_{mr}$ . A simple thought experiment of a worst case scenario bears this out. Assume that a Nova 2.1 is flying at 16.5 m/s into a 15.5 m/s headwind. At a resultant groundspeed of 1 m/s, it will take 100 s to cover 100 m, burning 4500 J. If that same Nova 2.1 were to fly at the upper limit of 30.5 m/s into the same 15.5 m/s headwind, the groundspeed would become 15 m/s. The sUAS now covers the same 100 m flight line in 6.6 s, burning only 957 J. Although the wattage required to maintain the faster airspeed is around four times higher, the overall energy consumption for the

flight line is lower. In addition to the obvious power consumption benefits, flying at higher speeds into the headwind also improves the time efficiency of data collection, as the time lost flying slower upwind without STF is not totally recovered during subsequent downwind legs. This effect will be discussed further detail in a later section.

Tailwinds will have the opposite effect, increasing effective groundspeed and necessitating a negative shift along the x-axis corresponding to the tailwind speed. As a result,  $V_{mr}$  will decrease from its still air value and the tangent line will become flatter, indicating an efficiency gain with lower DSEC.

As a rule,  $V_{mr}$  will always increase into headwinds and decrease into tailwinds. Although ever-increasing headwinds will necessitate higher and higher  $V_{mr}$  values until the vehicle's maximum power output is reached, ever-increasing tailwinds will not. Due to the parabolic shape of the power curve,  $V_{mr}$  values in increasingly strong tailwind conditions will decrease until they reach the lower bound indicated by  $V_{mp}$ , the minimum power airspeed. Further increases in tailwind speed will not necessitate further deceleration, but will still result in ground coverage improvements because of the increased groundspeed occurring at the minimum power level. In the unlikely event that the tailwind-enhanced groundspeed exceeds maximum allowable airbase limits, it will become necessary to fly slower than  $V_{mp}$  in order to maintain adequate image overlap. Crosswinds are compensated for by computing the effective geometric headwind/tailwind component and proceeding accordingly on the power curve (Arrow 1947).

### **Trailing Edge Control**

Because the high wind (10 m/s)  $V_{mr}$  for the Nova 2.1 fell near the maximum stable airspeed in the current flight envelope, an effort was needed to expand the high-speed

cruise capability of the sUAS to increase effective ground coverage in high wind conditions. Additionally, for lower-resolution, high-altitude mapping flights, it is more operationally efficient to fly as quickly as possible since forward image overlap is sufficient even at high speeds. This serves to maximize crew efficiency as it allows faster area coverage with the goal of enabling more flights per day on large survey projects (J. H. Perry 2011).

With a fixed trailing edge, the options for improving high-speed cruise for hand-launched sUAS are limited. Because the wing design must use a higher cambered airfoil to minimize launch incidents while maintaining a reasonable planform area, the minimum drag section  $C_d$  is inevitably higher than desired for high-speed cruise. As a result, the majority of the flight is spent in a suboptimal flight regime, paying a penalty required to satisfy the requirements of the first few seconds of flight.

Although flaps were omitted on the original-spec Nova 2.1 to save weight and operational complexity for unskilled operators, they were selected as a simple avenue to optimize the wing design for the wide airspeed range required for remote sensing applications. To provide a more direct comparison between wing designs, the wing planform was held constant and a simple airfoil substitution was made, replacing the original SD7032 with an MH32 foil, originally designed for pylon racers (Hepperle 1991). The two airfoils are visually compared in Figure 5-3, with the MH32's reduced thickness and camber immediately evident. Interestingly, many of the same design criteria for racing airfoils are common to remote sensing sUAS, namely a similar  $Re$  regime, low drag when flying fast, and strong performance when worked at high angles of attack.

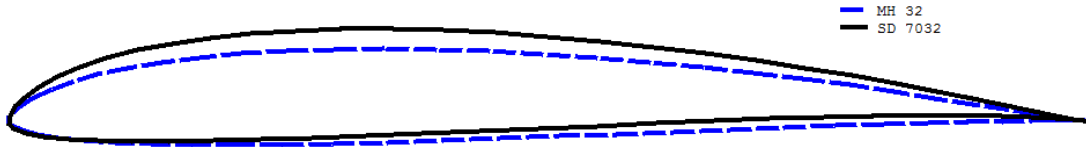


Figure 5-3. Visual comparison of SD7032 and MH32 airfoils.

An immediate inspection of the cruise ( $Re = 350k$ ) drag polars in Figure 5-4 reveals that although the SD7032 benefits from a higher  $C_{l,max}$  in a clean configuration, the MH32 performs much better in a high-speed cruise regime ( $C_l \approx 0.1$ ). This is a result of the new airfoil's lower thickness (8.66% vs. 9.96%) and camber (2.40% vs. 3.66%), which reduces its minimum drag  $C_d$  to  $\sim 0.2$  from  $\sim 0.5$  for the SD7032. Also, the MH32 is designed to be highly responsive to camber change, a trait not shared by the SD7032. This provides a significant benefit to STF optimization, because it provides an opportunity for fine wing adjustment for each commanded airspeed, rather than requiring large trailing edge deflections to established coarsely spaced flight modes.

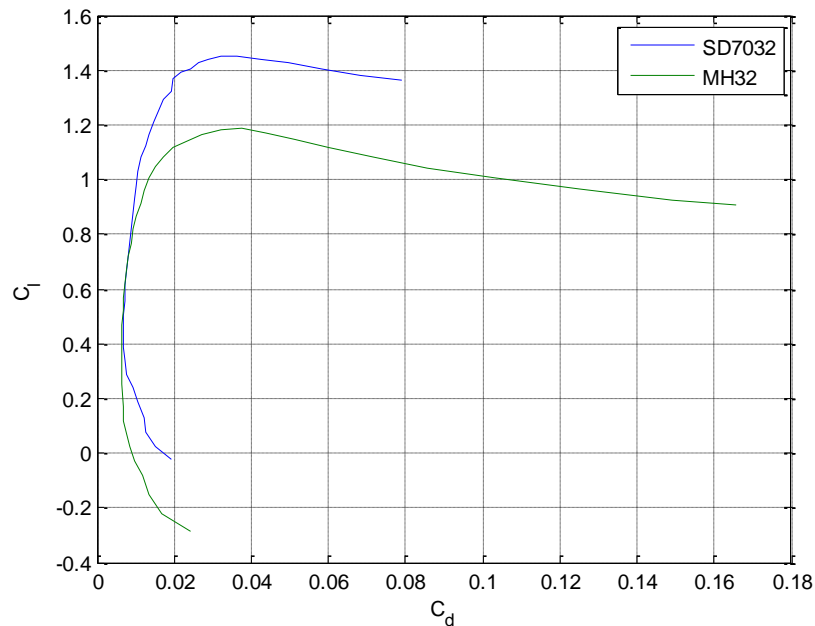


Figure 5-4. Comparison of drag polars ( $Re=350k$ ) for original SD7032 and MH32 airfoils.

By utilizing full trailing edge control (adjustable camber/reflex across inboard flaps and outboard spoilerons), the airfoil can then be dynamically modified in-flight to suit mission-specific airspeed requirements. For low-speed missions, the trailing edges are deflected down to provide increased camber and improved duration. As higher airspeeds are required, the trailing edge can be raised into a reflexed position, dropping excess camber and reducing drag for improved headwind penetration. Finally, these flaps are also deployed in a more typical manner to improve takeoff and landing performance and regain the high  $C_{l,max}$  offered by the original SD7032 configuration. A number of deflection geometries and their associated flight modes are presented in Figure 5-5.

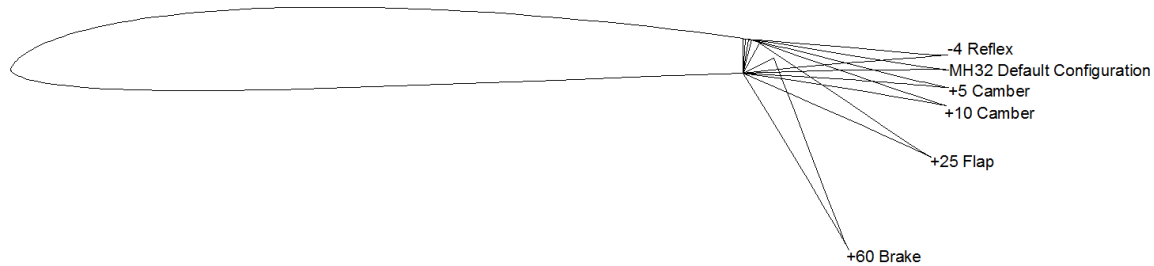


Figure 5-5. Trailing edge configurations for various flight mode settings.

With independently adjustable inboard and outboard camber settings, there is sufficient flexibility to finely tune the spanwise lift distribution to optimize the wing for each commanded airspeed or flight condition. This optimization was performed in XFLR5, with preliminary flight conditions focused on providing reduced power consumption in float, crawl, and dash modes. Independent inboard and outboard flaps also improve landing performance over simple inboard flaps or even full-span flaperons by enabling a butterfly landing configuration. This drops the inboard flaps to  $+60^\circ$  while raising the outboard spoilerons  $-15^\circ$ , generating a strong vortex at the panel junction in addition to the drag generated by the inboard flap deflection. The reduced effective angle of attack at the tip panels forces the center portion of the wing to stall first, promoting a straight-ahead stall that is much easier to recover from than a low altitude stall-spin event.

To recover the low speed, high lift performance provided by the previous SD7032 configuration, a takeoff flap setting was used, increasing the wing's overall  $C_{L,max}$  and preventing an increase in stall speed. Although the small camber and reflex deflections associated with the float and dash flight modes are not immediately visible, the larger flap changes for the takeoff and brake modes are shown in Figure 5-6, illustrating the flexibility provided by a four-surface wing.

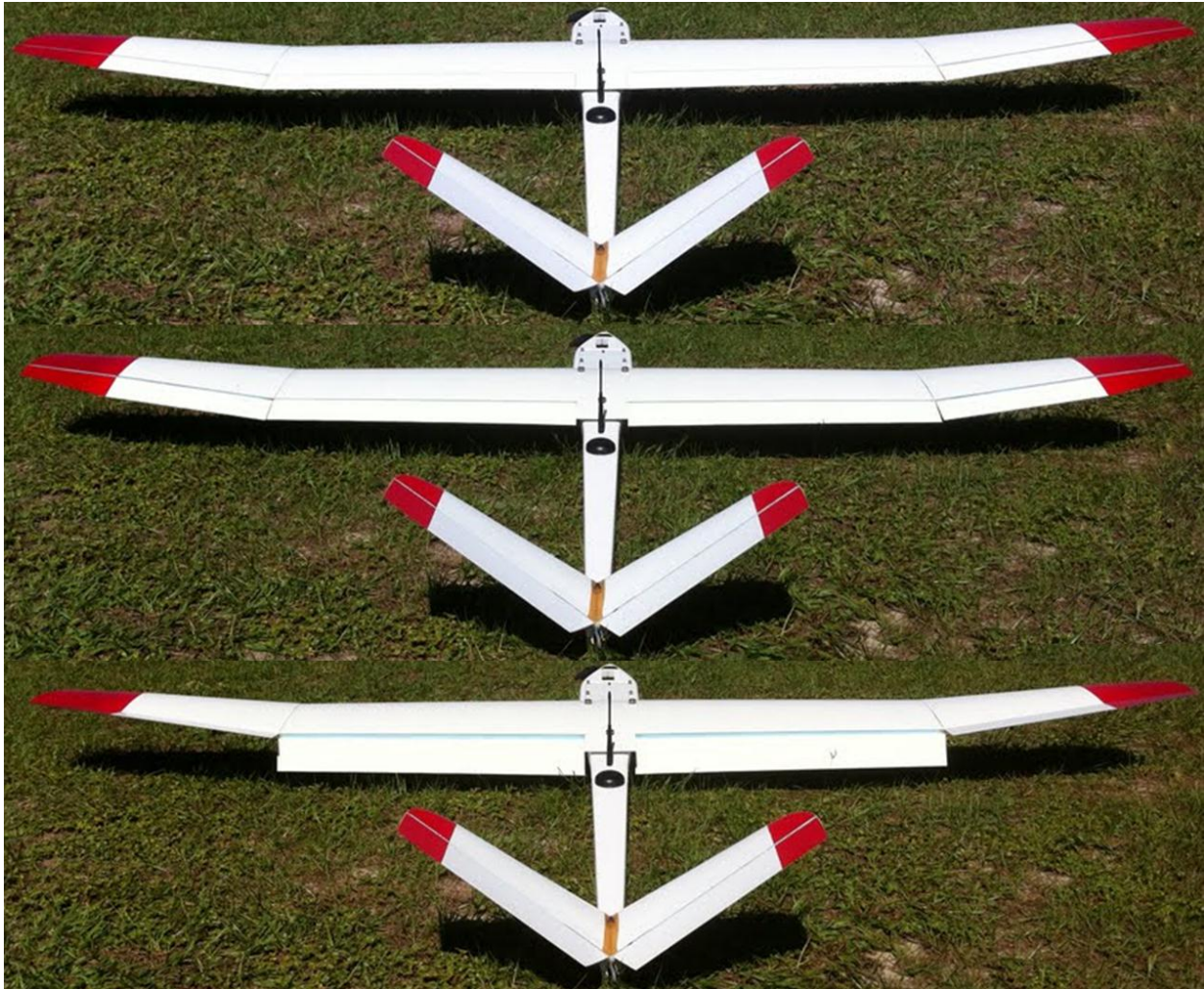


Figure 5-6. MH32 wing in clean, takeoff, and brake configurations. Camber change is especially noticeable at the inboard flap edges.

XFLR5 was used to generate performance polars for a range of potential wing configurations, applying a fixed lift (Type 2) analysis using the Nova 2.1 flying weight to determine cruise characteristics. Of the 30 flap configurations tested, three initial flight modes were selected, in addition to takeoff and brake configurations. These updated flap configurations, summarized in Table 5-1, improve the wing's performance across a broader speed range, improving slightly on the original power requirements in slow cruise while providing significant reductions in high-speed power consumption, especially in the reflexed dash mode. Although minor percentage gains could

theoretically be made by further subsetting the low speed flight regime with intermediate levels of camber, this was deemed unnecessary as the very minor gains only occurred across narrow speed ranges ( $\pm 0.5$  m/s). Additionally, while significant gains stand to be made at higher airspeeds ( $>30$  m/s) with increasing levels of reflex, the current power loading of the Nova 2.1 precludes flight at these speeds, primarily due to limitations in propeller pitch speed and the autopilot's climb algorithms.

Table 5-1. MH32 wing configuration parameters with flap deflections given in degrees, with positive values indicating downward deflection

Flap Mode	Airspeed Range	Inboard Deflection	Outboard Deflection
Brake	-	+60	-15
Takeoff	-	+10	+8
Float	9-13 m/s	+3	+2
Clean MH32	13-21m/s	0	0
Dash	21-30m/s	-1	-1

The computed drag polars for the original SD7032 configuration and selected MH32 flight modes are presented in Figure 5-7. Immediately evident is the significant drag reduction of the clean (no camber or reflex) MH32 configuration over the original Nova 2.1 wing at higher airspeeds ( $>16$  m/s), with further improvements available with the selection of the reflexed Dash configuration. Conversely, relatively uniform performance between the SD7032 and MH32 configurations is noted throughout the middle speed range (12-16 m/s), with the SD7032 having superior performance in the low speed regime due to its higher base camber level.

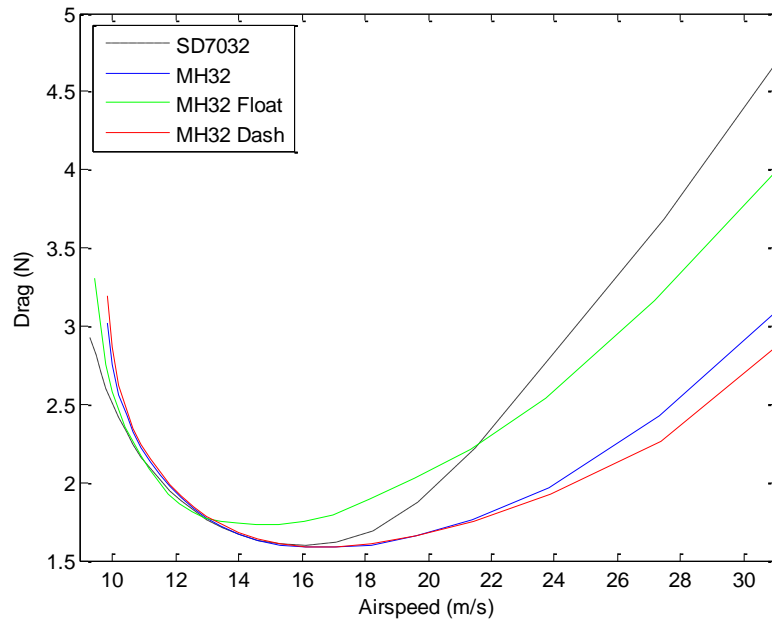


Figure 5-7. Computed drag curves for original SD7032 wing and MH32 wing in clean, float and dash modes demonstrating improved performance in high speed cruise.

These independent flight modes were then combined into a composite power curve, with the global minimum power consumption taken from each of the independent modes. The comparison between the original SD7032 configuration and the updated MH32 composite configuration presented in Figure 5-8 illustrates the dramatic effect dynamic camber adjustment can have across the flight envelope. The small upward kinks in the composite power curve between configurations indicate areas where intermediate adjustments can be made to further tailor the wing camber to better match the flight regime.

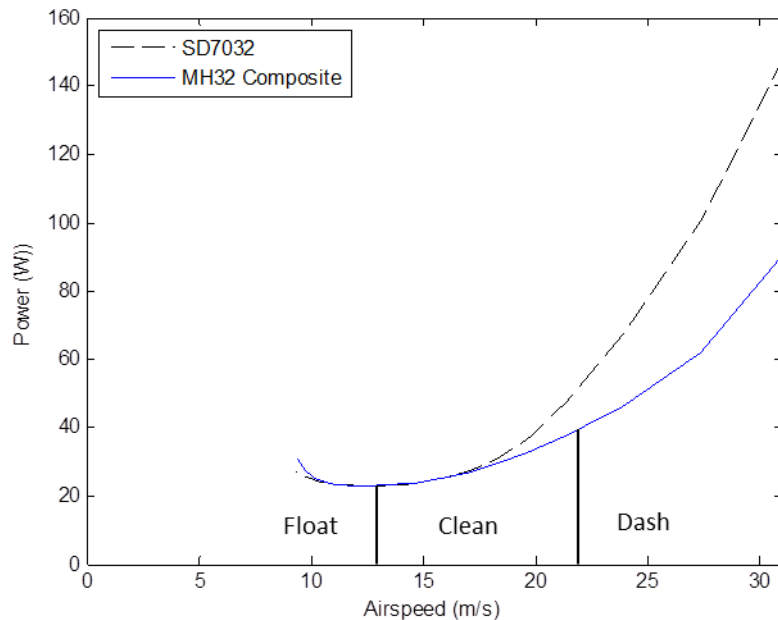


Figure 5-8. XFLR5-generated power curves for original SD7032 wing and composite curve for selected MH32 flight modes. The full selection of flight modes has been omitted for clarity.

Even without a complicated array of camber configurations, significant gains to flight efficiency can still be made by using only a few simple flight modes, and are readily integrated into most autopilot systems with minimal difficulty and mechanical complexity. These modifications not only improve global flight performance across the airspeed envelope, but prove especially beneficial for remote sensing applications where STF flight management strategies demand significant airspeed variations.

### Initial Power System Model

While preliminary power models generated using computed drag values and 100% propulsion efficiency assumptions are sufficient for comparative analysis between wing designs, greater fidelity is required to optimally integrate STF strategies. Towards this end, accurate power curves must be generated that incorporate appropriate efficiency models for all propulsion-related systems. Initially, efforts were made to determine these

power models computationally. Using a model described by the block diagram in Figure 5-9, estimated thrust requirements were combined with individual efficiency curves for the propeller, motor, and ESC to develop an overall relationship between cruise airspeed and required input power.

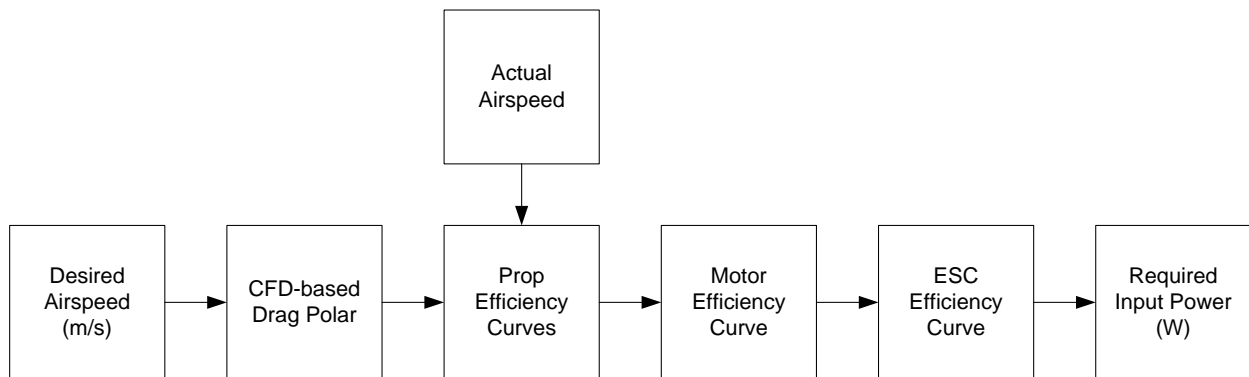


Figure 5-9. Power system block diagram.

Because little to no efficiency data are provided by manufacturers for any of the propulsion system components, a static thrust stand was constructed to provide a single model for the combined performance of the Nova 2.1 propeller, motor, and ESC. The results of the static thrust test are shown in Figure 5-10, with a maximum static thrust value of 31.1N yielding a takeoff thrust to weight ratio of 0.62. With the peak thrust significantly lower than predicted by the propeller RPM at that throttle setting, this indicates that the highly pitched 15x13 propeller is stalled, and limits the model's correlation with in-flight behavior.

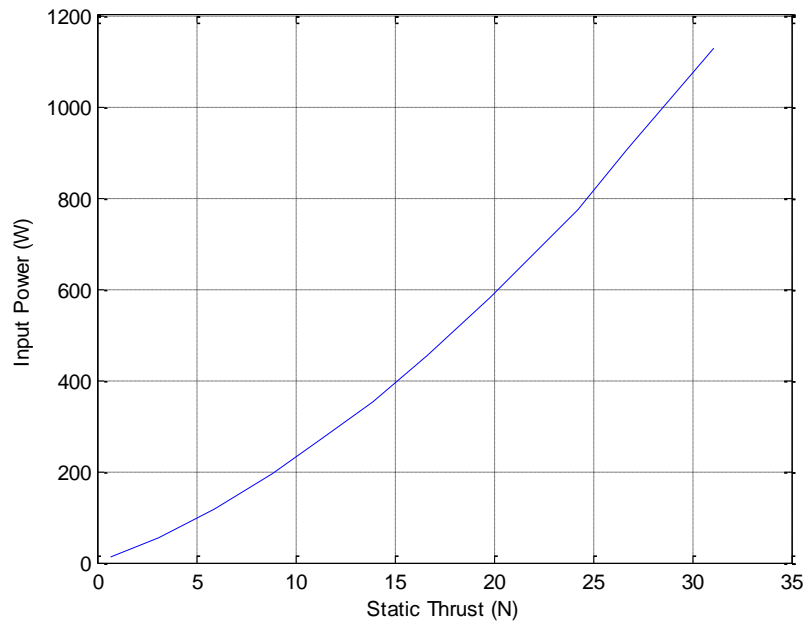


Figure 5-10. Static thrust test results for Neu 1509/1.5Y (6.7:1 GB), Phoenix Ice 100, Aeronaut CAM 15x13 folding prop.

Full estimation of the propeller efficiency at various airspeeds is a complicated affair requiring collection of thrust and power measurements to determine appropriate performance coefficients,  $C_T$  and  $C_P$ . Used in Equations 5-2 through 5-4, these parameters also require knowledge of advance ratio,  $J$ , which must be collected in-flight. As a result, thrust values found for static tests are insufficient for accurate efficiency calculations.

Propeller thrust coefficient,  $C_T$

$$C_T = \frac{T}{\sigma n^2 D^4} \tag{5-2}$$

Propeller power coefficient,  $C_P$

$$C_P = \frac{P}{\sigma n^3 D^5} \tag{5-3}$$

Propeller efficiency,  $\eta$

$$\eta = J \frac{C_T}{C_P}$$

(5-4)

The shortcomings of the power estimation were not limited to an inadequate propeller model. Combining the thrust stand results with the computed drag curves previously described in Figure 5-7, an estimated power model for the Nova 2.1 was generated, and a test flight was conducted for validation purposes. During the flight, autopilot-stabilized flight lines were flown at fixed airspeeds, and the level flight power consumption was measured. The results of the model's comparison with this preliminary experimental data, shown in Figure 5-11, demonstrate the significant disagreement between simple calculations and real-world results.

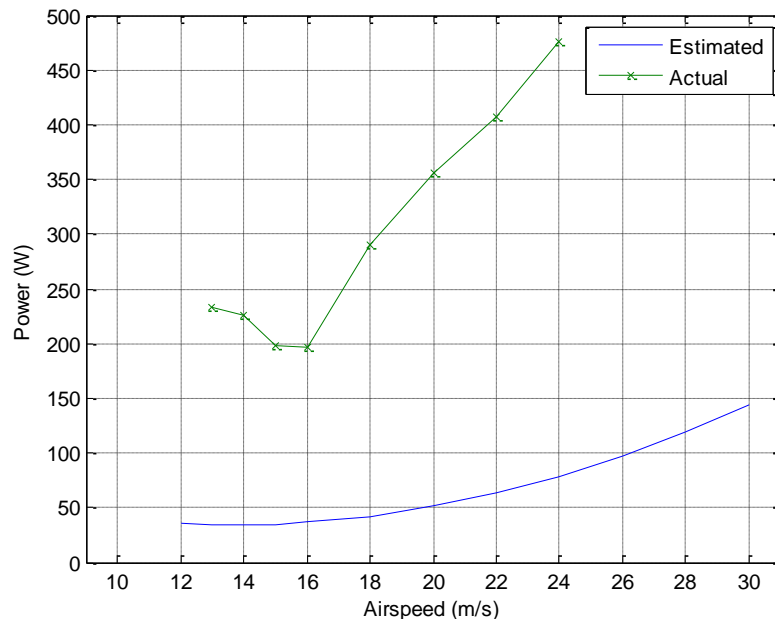


Figure 5-11. Comparison of computational power curve model with experimental values for original SD7032 wing.

Although computational models like those used in XFLR5 nearly always under-predict drag, it was found that the primary contributor to the experimental disagreement with the model power curve was the frequent and irregular power spikes encountered as the autopilot modulated the throttle to maintain each commanded airspeed. While this can be somewhat minimized through optimal tuning of throttle-slew rates, it comes with the tradeoff of poorer airspeed and altitude tracking. The irregularity of these throttle spikes, coupled with related throttle ‘noise’ due to atmospheric disturbances like thermal up/downdrafts, prevented the determination of an accurate correction function. As a result, all further efforts turned to generation of experimentally obtained power curves that better match real-world performance.

### **Experimental Power Consumption Testing**

To gather in-flight power consumption information, an Eagle Tree Systems® eLogger™ V3 was utilized to record system voltage and current draw. Connected in-line just after the system battery, this configuration allowed the additional monitoring of payload and autopilot baseline power requirements that, although minor, have measurable impacts on overall system duration. These values were recorded at a 2 Hz rate and synchronized with logged RPM data from the ESC and telemetry recorded by the Kestrel™ autopilot after each flight. Experimental power data for the Nova 2.1 system was collected by flying numerous linear transects at constant, autopilot-controlled airspeeds while energy consumption rates were measured. In keeping with FAA-mandated VLOS restrictions, the transects were limited in length to 1.6 km, as shown in the ground station screenshot in Figure 5-12.

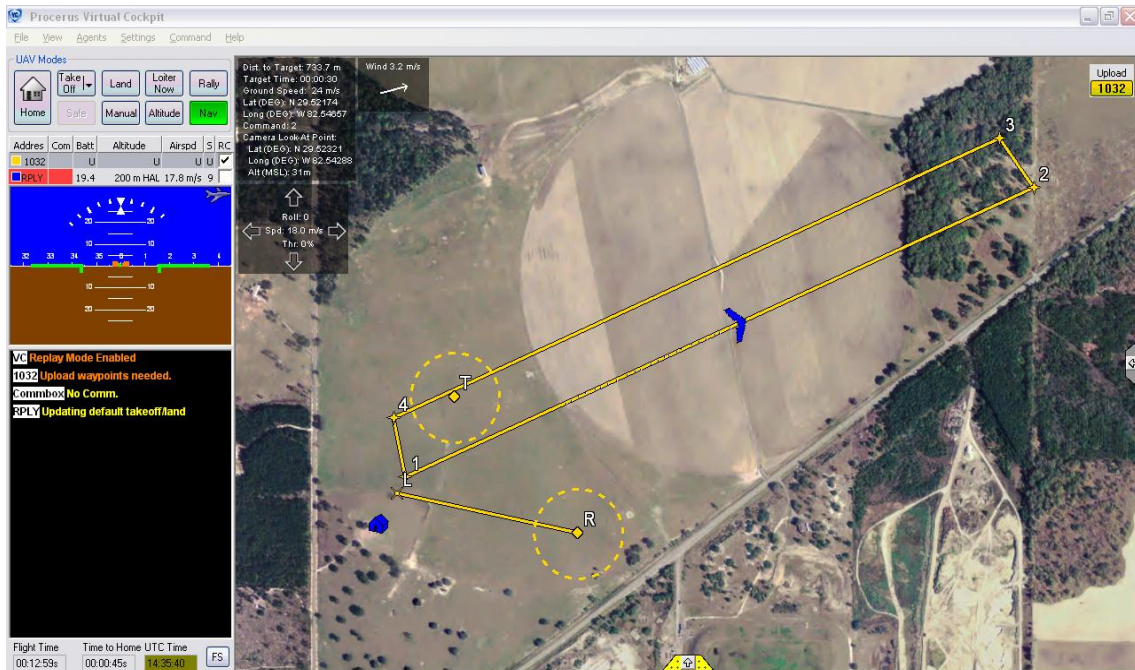


Figure 5-12. Power testing flight plan consisting of repeated 1.6 km long parallel transects.

Care was taken to minimize the effects of thermal updrafts and, following a linear regression on the initial data set, a three-sigma rejection criteria was utilized to reject possible outliers. These flights were also performed with the payload running, which contributes a constant power draw of ~6.5 W, giving real-world numbers that are much more valuable for practical flight planning purposes.

Including reflights due to thermal interference, a total of 6 data collection flights, each roughly 50 minutes in duration, were flown to collect power data for the SD7032, MH32 Clean, MH32 Float, and MH32 Dash configurations. Because both test wings fit interchangeably with the Nova 2.1 fuselage, the remainder of the system configuration could be held constant between flights to provide a direct comparison. A sample power profile for an MH32 Clean test flight is presented below in Figure 5-13. The commanded airspeeds for this flight are also plotted to indicate the relative timing of each airspeed

window, and the stable staircase behavior of the power indicates acceptable overall tracking. The spikes visible at the ends of each airspeed interval correspond to required accelerations, while the brief peaks at the middle of each window are correlated to the 180° turnaround at the end of the transect.

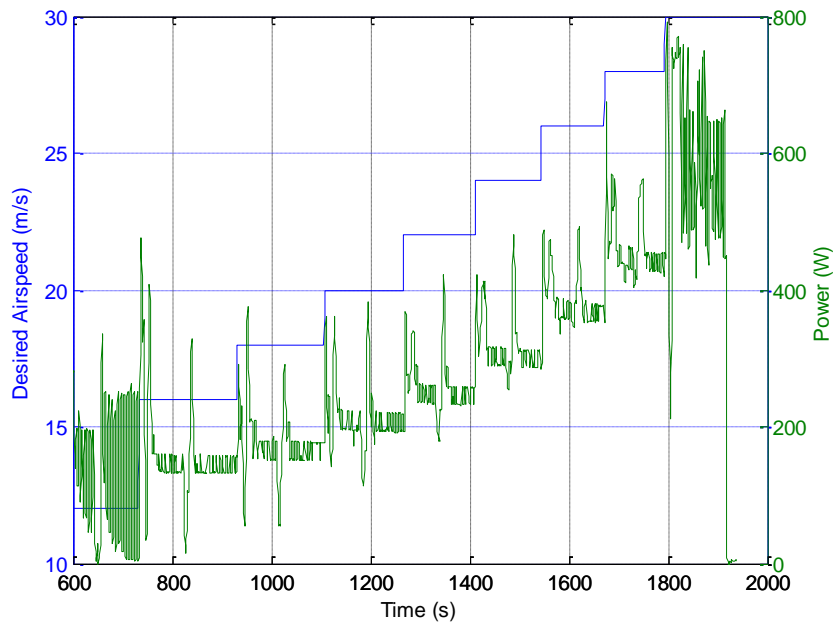


Figure 5-13. Airspeed intervals for MH32 clean configuration flight.

To process the collected power data, each commanded airspeed was considered achieved when the autopilot telemetry indicated that the aircraft had reached the new commanded airspeed and held steady within 0.5 m/s while not varying altitude by more than 2 m for at least 2 seconds to reject over- and undershoots as the airspeed stabilized. When this was not achievable, typically due to phugoid instability at the high and low ends of the airspeed range, the data for that airspeed was omitted and that configuration’s airspeed range adjusted accordingly. This limit is mainly a result of the Kestrel™ autopilot’s lack of gain scheduling, and has motivated the investigation into alternate autopilots to expand the Nova 2.1’s available operating window.

The experimentally derived power consumption data, presented in Figure 5-14, compares the original wing with selected configurations of the updated flapped variant. As expected, the updated base MH32 wing showed improved high speed performance over the original design, even expanding the available airspeed envelope from 24 m/s to 30 m/s before pitch instability or climb faults became a factor. Additionally, reduced high and low speed power consumption was achieved in Dash and Float flight modes. Decent agreement between the predicted crossover points on the power curves was observed, as the Dash configuration began surpassing the base MH32 wing at 22 m/s (21 m/s was predicted). Similarly, the performance transition towards the Float configuration occurred at 17 m/s, slightly faster than the predicted 13 m/s.

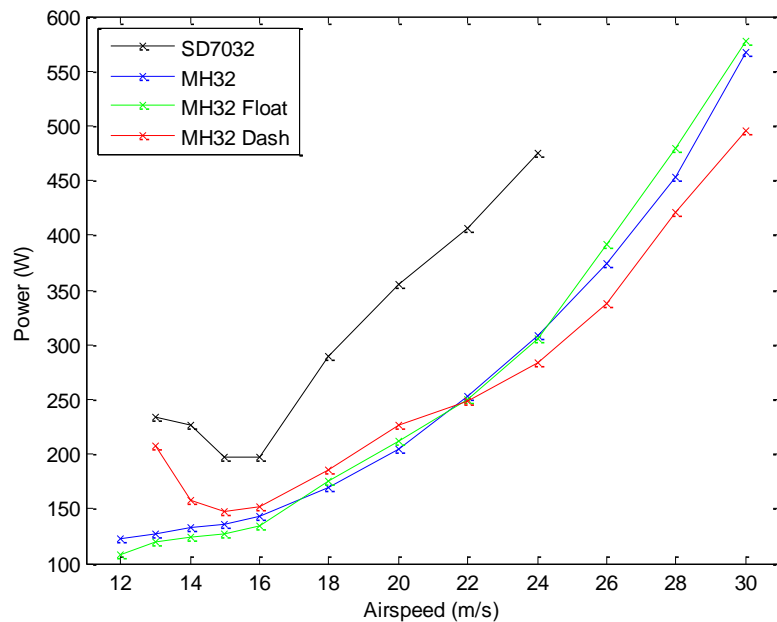


Figure 5-14. Experimentally derived power consumption results compared for original Nova 2.1 wing and modified MH32 configurations.

Surprisingly, even the low speed performance of the SD7032 showed much poorer performance than the updated wing, even after reflights to confirm the unexpected result. These higher power consumption rates are associated with poor airspeed

tracking, observed as significant throttle variations that occur even during straight-and-level transects. This unsteady throttle input, with variations of up to 40%, was much higher than observed during flights of the updated wing, where level-flight throttle inputs were frequently held  $\pm 5\%$ . The resulting power data, shown in Figure 5-15, would initially hint at poor tuning. This is surprising, considering that the throttle tracking is even noticeably poor in the middle of the airspeed range, which is the regime around which the Kestrel™ autopilot was initially tuned.

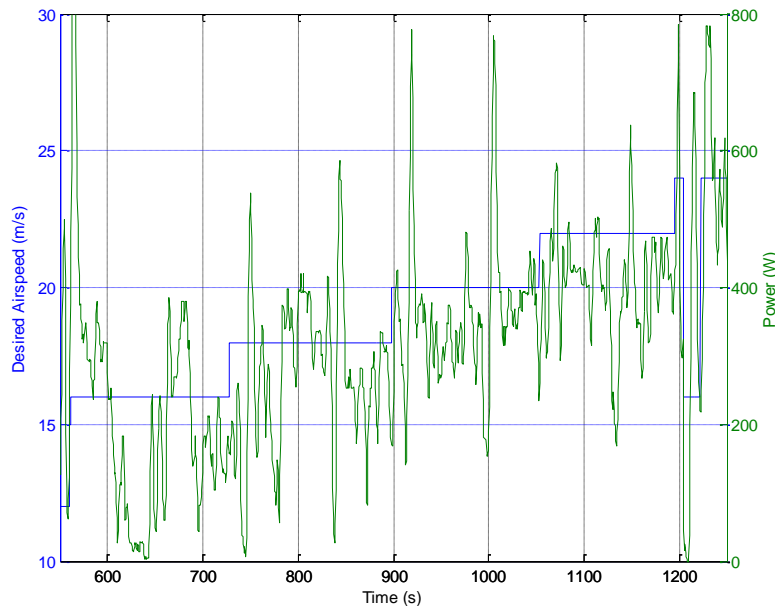


Figure 5-15. Airspeed intervals for SD7032 configuration flight showing much noisier data and a climb fault occurring during a 24 m/s transect.

By combining airspeed data with logged RPM values throughout the flight, propeller selection for cruise optimization can be evaluated by computing the average operating advance ratio,  $J$ , encountered during normal airspeeds for remote sensing use. As discussed in previous sections, the propeller's  $P/D$  ratio should approximately match  $J$  ( $\sim 0.1$  less according to Figure 3-15) in order to provide the optimum propulsive efficiency. With variation in  $J$  across the airspeed range shown for a clean MH32

configuration in Figure 5-16, the average advance ratio for all MH32 flight modes was found to be 0.77. With the nearest propeller choices being 15x13 ( $P/D = 0.857$ ) and 15x10 ( $P/D = 0.660$ ), the selected Aeronaut 15x13 CAM propeller is the best available option for cruise optimization. Finally, although the 15x10 would offer a considerable static thrust advantage for hand-launch improvements and may be better suited for slower ISR flights, the higher speeds available for STF integration confirm the 15x13 as a superior choice for sUAS-based remote sensing applications.

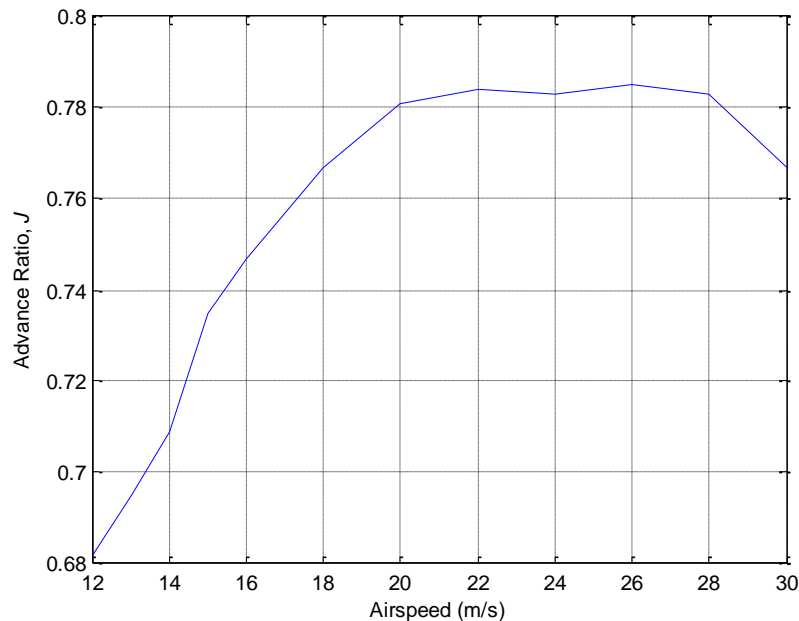


Figure 5-16. Variation of advance ratio,  $J$ , across airspeed range for MH32 clean configuration.

### STF Application

To verify the effectiveness of STF application to flight management, experimental power curves for the clean MH32 and camber-adjusted variants were used, allowing simultaneous evaluation of predicted improvements to STF due to integration of camber change. To better illustrate the deleterious effects steady winds have on aerial mapping flights, simulated transects over a 2 km long target area will be evaluated for both time-

of-flight and energy requirements. First, the experimental power curve for a fixed-camber MH32 wing, presented in Figure 5-17, is considered.

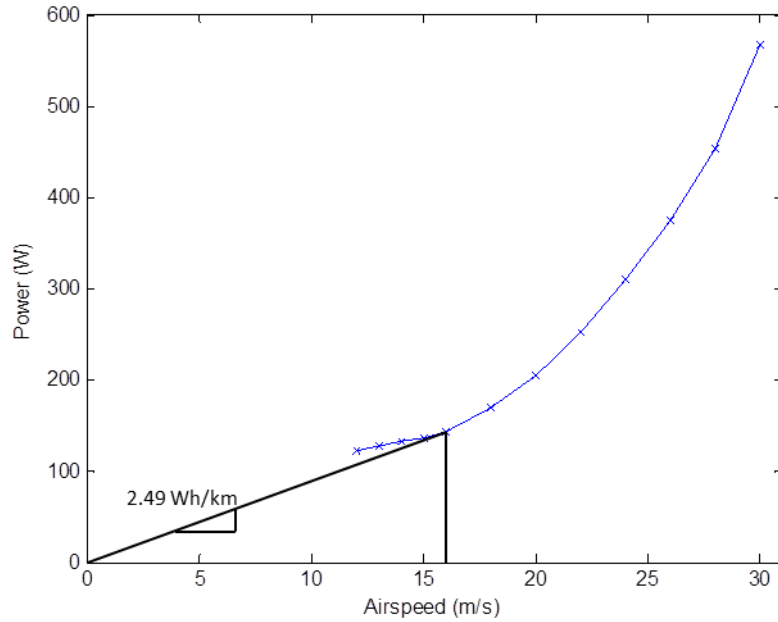


Figure 5-17. Experimentally obtained MH32 power curve with still air DSEC shown.

From inspection,  $V_{mp}$  in this configuration falls at 12 m/s, with a corresponding 122.4 W average power draw. In zero wind conditions,  $V_{mr}^*$  for this particular wing falls at 16 m/s, yielding a DSEC of 2.49 Wh/km. A sample pair of 2 km long transects (upwind and downwind legs) flown in these conditions will require 4 minutes, 10 seconds and 9.96 Wh of energy to complete, as shown in Figure 5-18.

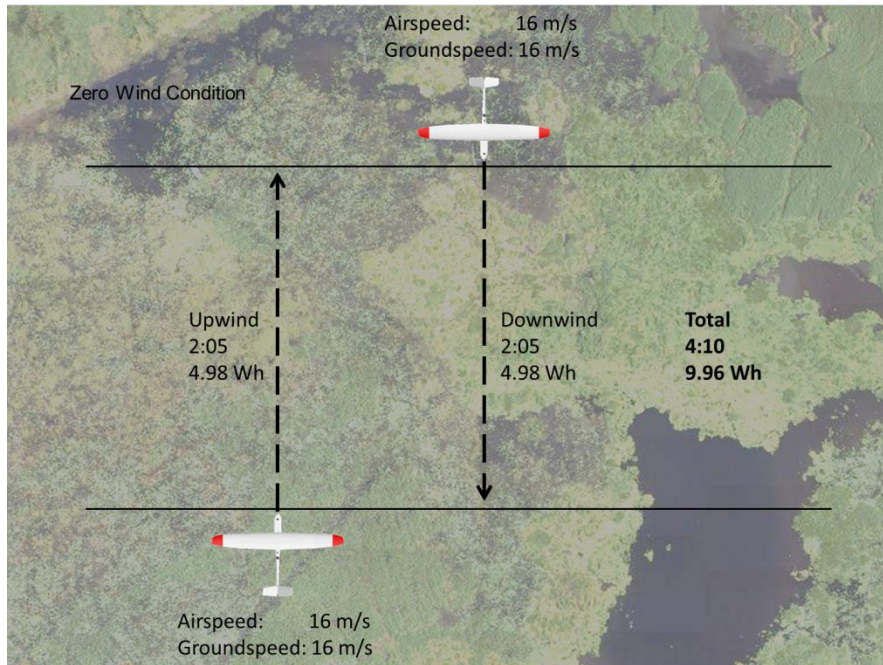


Figure 5-18. Schematic of flight performance for 2 km transects in still air conditions detailing time of flight and power consumption.

If, for the same configuration, a steady 10 m/s wind were encountered and the commanded airspeed went unchanged in response, significant time and energy penalties would ensue, as summarized in Figure 5-19. During the upwind leg, effective groundspeed will be reduced to 6 m/s, dramatically increasing the time-of-flight and raising the DSEC to 6.63 Wh/km, a 266% increase over the still air figure. Although the downwind leg will proceed much faster, with an effective groundspeed of 26 m/s, the overall time-of-flight for the pair of transects is increased over the still air figure by 65%. Similarly, the reduced DSEC of the downwind leg fails to make up for the losses encountered during the upwind transect, resulting in a total power consumption of 16.32 Wh, an increase of 64%. Additionally, the high groundspeed encountered on the downwind leg may exceed minimum airbase requirements, resulting in still-larger efficiency losses as only upwind legs become usable for data collection.

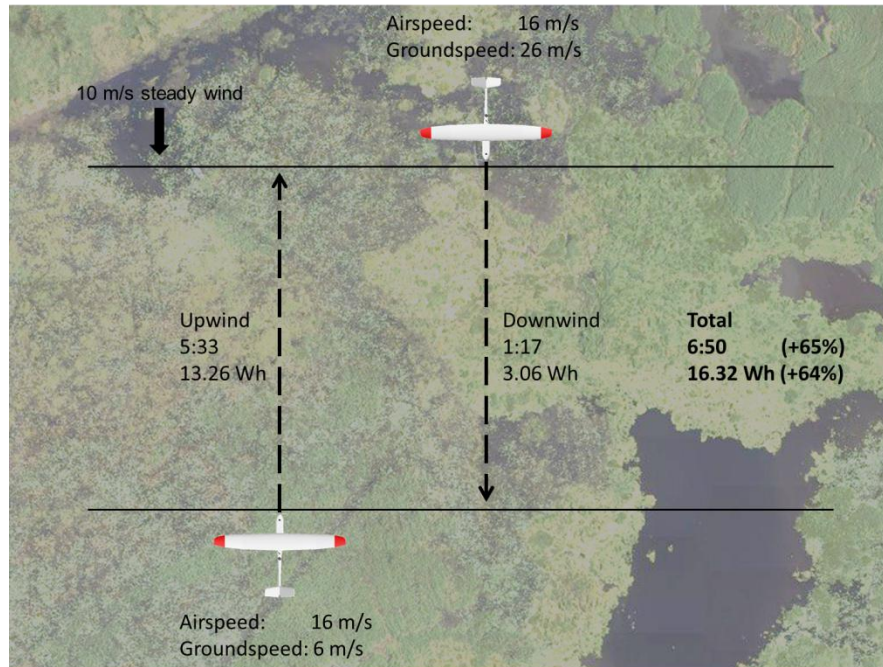


Figure 5-19. Schematic of flight performance for 2 km transects in 10 m/s steady wind conditions, illustrating efficiency losses without STF application.

To minimize these losses, application of STF strategies begin by reexamining the aircraft power curve. With the example 10 m/s headwind, the new value for  $V_{mr}$  rises to 20 m/s, with a headwind-reduced DSEC of 5.69 Wh/km, presenting a 14% improvement over the previous non-STF upwind case. For the downwind leg, STF application requires that the Nova 2.1 now fly at  $V_{mp}$  (12 m/s). The resulting flight plan with relative gains over the non-STF case is presented in Figure 5-20. By applying STF strategies, a total time-of-flight reduction of 29% and a total energy savings of 11% were achieved relative to the unmodified flight plan, demonstrating significant operational advantages to the technique.

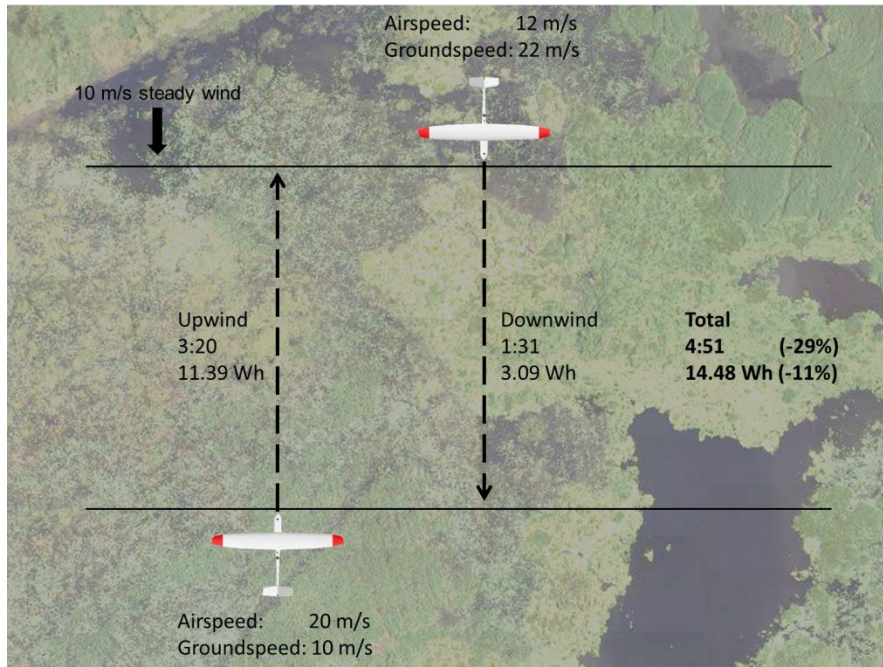


Figure 5-20. Improved time and ground coverage efficiencies for 2 km transects in 10 m/s steady wind with STF application.

Through variable camber integration into STF application, minor additional gains in both time and energy consumption will also be possible. For this analysis, the composite MH32 power curve in Figure 5-21 is used to compute appropriate flight speeds for both the headwind (red line) and tailwind (black line) conditions. At both airspeeds, the lower position of the composite power curve demonstrates an efficiency gain over the fixed camber MH32 variant.

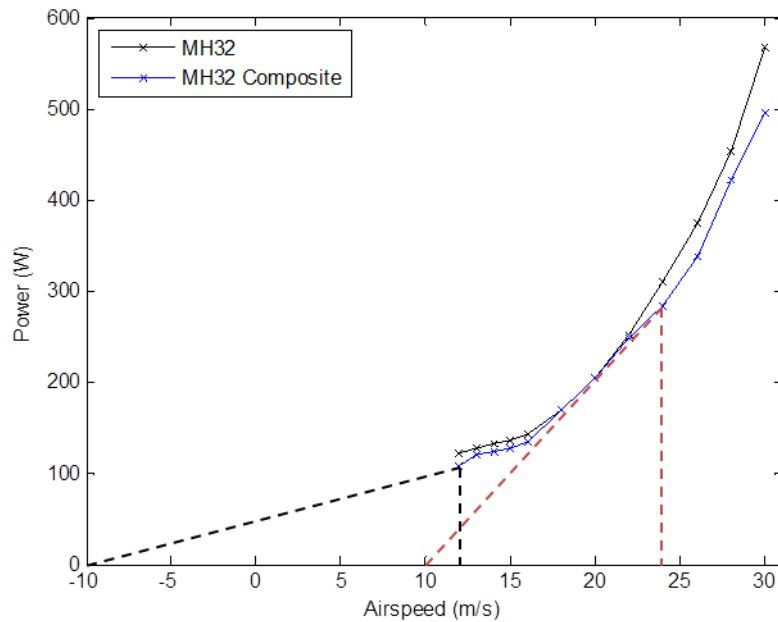


Figure 5-21. Demonstration of performance gains using variable camber enhanced STF on MH 32 composite power curve.

During the upwind leg of the transect, the wing is set in its Dash position, enabling the Nova 2.1 to penetrate upwind at a  $V_{mr}$  of 24 m/s. Although only slightly more efficient than the fixed camber case with respect to energy consumption, this increased speed reduces the time-of-flight by nearly a minute, and contributes to the entirety of the 20% flight time reduction for this example. During the downwind phase, the flight speed remains the same, pegged at a  $V_{mp}$  of 12 m/s. However, because the wing can be set into the more efficient Float configuration for this airspeed, a small power savings can also be obtained. As summarized in Figure 5-22, although camber adjustment offers only slight reductions in overall energy consumption (3%) over the fixed configuration STF example, the increased airspeed range results in significant time savings, so much so that the total time is less than that of the initial zero wind case.

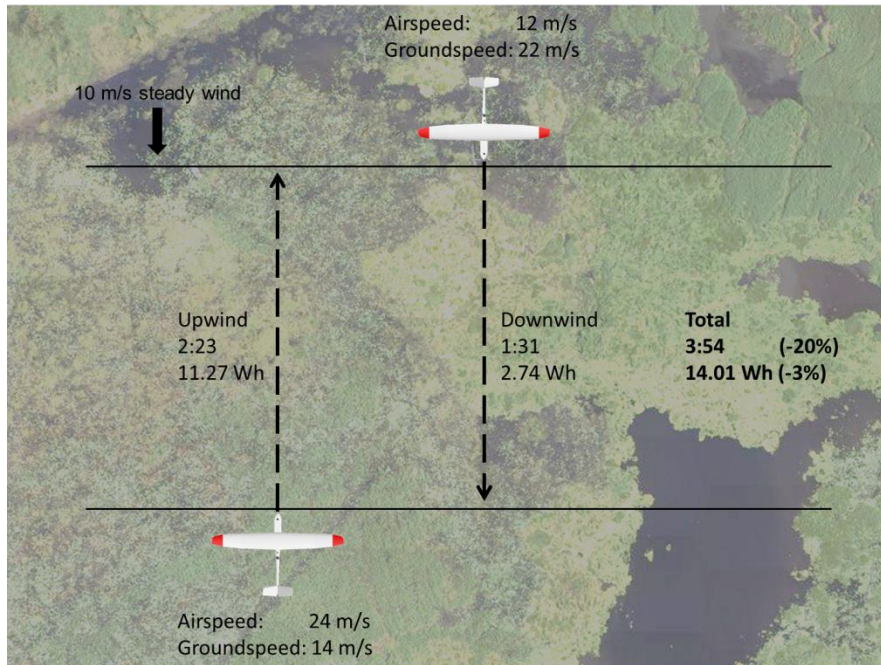


Figure 5-22. Schematic of flight performance with variable camber enhanced STF application.

Although STF with variable camber has the greatest effect with high wind speeds, it can still offer modest (6.5%) reductions in DSEC even in zero wind conditions. In addition to the additional ground coverage offered by STF integration, a somewhat unexpected benefit is found in the dramatically reduced time of flight for mapping operations. For large projects, this is hugely important, as it reduces total deployment time, offering significant logistical and financial incentives

With variable camber and application of STF now justified for both upwind and downwind components, the question arises of scalability. Are STF strategies practical for commercial or civil aviation? Probably not, since the cruise speeds for both are typically much higher than the prevailing wind speed for any given flight. While the theory still holds true, the efficiency gains of using STF are marginal for a vehicle whose  $V_{mp}$  is often an order of magnitude higher than the prevailing wind. Additionally, unlike

civil and commercial flights whose routes are predefined based on destination, optimal aerial mapping flight plans orient all flight lines in the same direction of the wind, allowing for maximum implementation of STF theory. Furthermore, the small distance scale of an sUAS flight causes the local wind field to appear semi-constant, whereas the effective wind field for a commercial flight will be much more varied, lending itself to alternative flight planning strategies to take benefit of regionally favorable wind conditions (Rubio and Kragelund 2003).

An additional consideration for the suitability of STF strategies is the degree to which power consumption increases with speed. The sharper the power consumption curve, the larger the effect will be on the slope of the energy-per-unit-distance line. The  $1/x$  efficiency curve for electric power systems is quite different from wet fueled engines, which tend to have a flatter, more linear power curve and don't pay such an energy penalty for off-peak operation. As a result, STF is most effective when  $V_{mp}$  is within an order of magnitude of the wind speed. This is most pronounced in gliders, High Altitude Long Endurance (HALE) UAS, and sUAS applications. Surprisingly, even migratory birds display this behavior of slowing down to  $V_{mp}$  in tailwinds and accelerating to  $V_{mr}$  in headwinds (Alerstam 1990).

### **Autopilot Integration of Variable Camber for STF**

Integration of STF theory into the current flight path navigation algorithm is relatively straightforward. The same avionics equipment mentioned above is used, with the exception of custom firmware for the Kestrel™ to give more precise control of both inboard and outboard control surfaces. With this firmware, complete independent control of each surface is granted to the autopilot, essentially creating an infinite number of discrete configurations (over  $2 \times 10^{100}$  with integer-resolution deflection settings).

In an effort to prevent this flight management strategy from creating a controls issue, flap integration was accomplished with an open loop controller for surface deflection. This meant that flap deflection was not continuously varied in response to normal airspeed fluctuations, but remained in specified configurations based on commanded airspeeds. For additional safety, latching was implemented to prevent inadvertent flap reconfigurations that are dangerous to flight. In this approach, a discrete controller is used with cruise, acceleration, and deceleration modes. During acceleration mode, when the desired airspeed is more than 4 m/s greater than the current airspeed, the flaps will incrementally retract as airspeed increases. This prevents the flaps from retracting prematurely and causing a stall. Conversely, in deceleration mode, when the commanded airspeed is more than 4 m/s less than the current speed, the flaps will incrementally extend as airspeed decreases. This also prevents a premature stall from commanded airspeeds lower than the flaps-deployed stall speed. Once the vehicle is within 4 m/s of the desired airspeed, the cruise latch is triggered, automatically transitioning the aircraft out of acceleration or deceleration mode. During cruise mode, once the flaps are in their airspeed-appropriate configuration, they will not move until a different commanded airspeed is given. Using this method, each discrete airspeed or airspeed range can be paired with an optimized flap setting to provide improved cruise efficiency to the limit of the wing design.

This implementation strategy avoids the undesirable positive feedback loop associated with closed loop flap control. Without this strategy, wind gusts or other perturbations could cause undamped oscillations as shown in Figure 5-23. If a Nova 2.1 were cruising at a desired airspeed of 15 m/s and a perturbation occurred to cause the

airspeed to dip below 15 m/s, closed-loop control would cause flaps to extend, further slowing the aircraft. Shortly thereafter, the throttle would increase effort in response to the increasing error between actual and commanded airspeeds. When this additional power increases the airspeed, flaps will retract in response to a new optimal condition. The sudden decrease in drag will then cause the airspeed to increase even further before the throttle decreases, causing overshoot. This underdamped positive feedback loop currently rules out closed-loop flap control integration at this time.

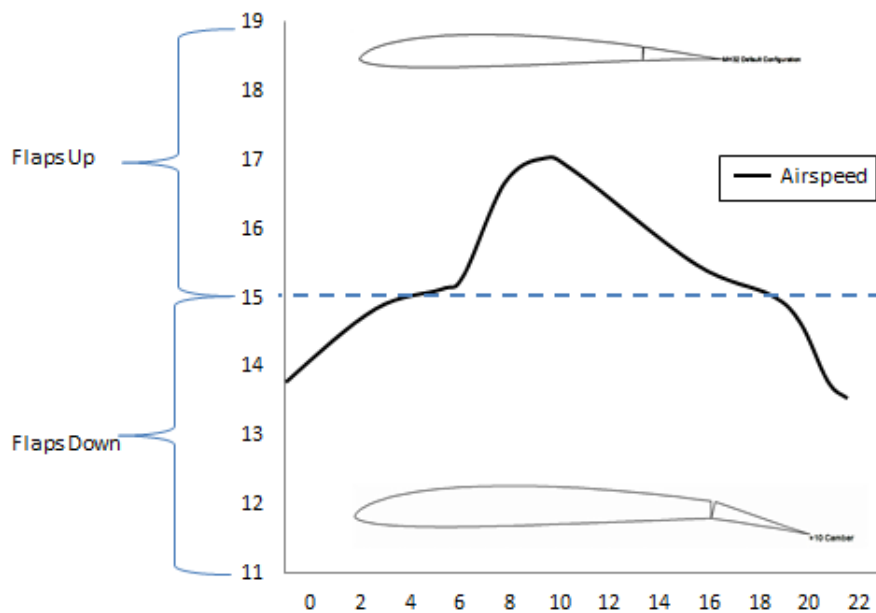


Figure 5-23. Positive feedback in closed-loop flap control.

Full mission camber optimization must also account for the takeoff and landing phases of flights. During the first phase of takeoff, any STF logic is disabled and a constant takeoff flap setting is desired. This is to prevent premature flap retraction in cases of wind gusts and ground effect below the flaps-deployed stall speed. Similarly, cruise-optimized STF logic should also be overridden during landing. During the initial descent phase of the landing procedure, takeoff flaps are again deployed, maximizing

available lift to lower the stall speed while also increasing drag to increase the descent angle. Following the transition to a final landing approach, full brake is deployed, extending both inboard flaps and outboard spoilerons to decelerate and descend as quickly as possible, maximizing landing performance to enable short field operations. During initial tests, full brake deployment resulted in a decrease in required final approach distance of over 50%, with more improvements available with improved tuning and more aggressive final routing.

## CHAPTER 6 SUMMARY AND CONCLUSIONS

### **Summary**

The purpose of this thesis was to determine an appropriate sUAS design process to optimize overall system effectiveness for emerging remote sensing applications. Towards this end, a logical hierarchy of system design constraints was developed from desired output data specifications, payload limitations, and the realities of operational deployments. The initial development and operational assessment of the Nova 2.1 sUAS was examined, with special focus on its suitability for aerial mapping applications. To further improve the feasibility of deploying sUAS for remote sensing applications, various strategies to enhance the efficiency of flight path management were explored. Due to the unique power constraints of electric-powered sUAS, significant importance was placed on overall energy management through the minimization of unnecessary mission overhead.

In an effort to improve ground coverage efficiency throughout the main data collection portions of aerial mapping flights, both in terms of flight time and overall mappable area, speed to fly theory was incorporated into the Nova 2.1 flight management package. By optimizing flight speeds based on current wind conditions, significant improvements could be made in overall ground coverage efficiency. To further improve the Nova 2.1 system for its target applications, trailing edge control was integrated into the STF algorithm in addition to the general operation of the system, reducing cruise drag and improving takeoff and landing performance.

## **Conclusions**

Building upon five generations of institutional experience developing sUAS for remote sensing applications, the Nova 2.1 was the first aircraft in its class capable of providing high accuracy, high resolution geospatial data products on an operational basis. Due to the implementation of a design process focused on eliminating operational deficiencies, the Nova 2.1 proved highly successful during the last two years of field deployments by crews within the UF UASRG as well as external operators within the USACE.

While initial integration of overhead minimization strategies was limited to on-the-fly adjustments by the ground station operator, updated flight management software has been developed to automate much of this process, resulting in a 20% reduction in energy consumption during the beginning and terminal phases of mapping flights. Following power consumption test flights for the original wing as well as an updated flapped variant, STF application was found to offer up to 14% increased ground coverage and a 43% reduction in required flight time for mapping flights in high wind conditions. Additionally, camber adjustment was shown to significantly increase available airspeed range, widening the operational envelope for a variety of sUAS applications. Finally, preliminary integration of a landing flap configuration reduced the Nova 2.1's autonomous landing length requirement by 55%, reducing deployment requirements and improving operational availability in challenging terrain.

## **Recommendations**

A natural product of continued operation of a complex system like a remote sensing sUAS is the constant cycle of improvement that occurs as new applications give rise to novel problems. Currently, remote sensing missions using the Nova 2.1

sUAS require extensive operator experience, not for the safe navigation of the aircraft, but rather to ensure that usable data are being generated with each flight. Because of the steep learning curve associated with effective flight planning for aerial photogrammetry applications, a number of initial missions were completed successfully, yet produced no usable data due to insufficient stereoscopic coverage or similar technical issues that precluded postprocessing of collected imagery. To improve the feasibility of widespread use of sUAS as remote sensing tools, flight planning should be automated as much as possible until only the most basic user inputs are required. In an ideal situation, an operator would only need to input their desired data product specifications and provide an outline of the target area in order to generate an optimized flight plan, with all relevant payload control also being managed internally to the system.

To ensure that the maximum performance capabilities of a given sUAS are utilized to provide the highest operational capacity for remote sensing applications, integration of STF strategies should be designed in from the start. On the airframe side, this means taking full advantage of the additional flexibility afforded by fully variable camber to keep overall wing area small, both for high speed cruise and practical packing considerations. Regarding autopilot development, work should continue towards providing hands-off STF optimization of flight speeds and wing configurations throughout the flight without external operator input, as existing implementations currently require. As with flight planning, efforts should be focused on moving all major mission management to the software backend wherever practical.

Finally, to improve operational flexibility, the internal autopilot control algorithms should be modified to allow gain scheduling, which would permit a wider operational

airspeed envelope and allow more accurate control with large flap deflections. While the latter certainly limits overall takeoff and landing efficiency, the actual routing of takeoff and landing flight paths can also limit absolute performance. To improve overall takeoff and landing performance, these flight paths should be made much more aggressive to reduce operating area requirements, alleviating what is currently a primary operational limitation of the Nova 2.1 system.

## LIST OF REFERENCES

- Abbott, I., and A. Von Doenhoff. *Theory of Wing Sections: Including a Summary of Airfoil Data*. Courier Dover Publications, 1959.
- Alerstam, T. *Bird Migration*. Cambridge University Press, 1990.
- Anderson, J. D. *Fundamentals of Aerodynamics*. McGraw-Hill, 2007.
- Arrow, K. "On the Use of Winds in Flight Planning." *Journal of Meteorology*, 1947.
- Bowman, W. S. "Design and Validation of Autonomous Rapid Mapping System Using Small UAV." *Master's Thesis*. University of Florida, 2008.
- Bowman, W. S., A. C. Watts, J. H. Perry, M. Morton, and P. G. Ifju. "UAS as monitoring tools for assessing the Nation's levees and monitoring invasive plant populations." *Workshop held at the US Army Corps of Engineers Research and Development Center*. Vicksburg, MS: Presentation slides, March 19, 2008.
- Breckenridge, R. "Improving Rangeland Monitoring and Assessment: Integrating Remote Sensing, GIS, and Unmanned Aerial Vehicle Systems." *Dissertation*. University of Idaho, 2007.
- Breckenridge, R., J. Harbour, R. Lee, M. Dakins, and S. Bunting. "Using Unmanned Aerial Vehicles to Assess Vegetative Cover and Identify Biotic Resources in Sagebrush Steppe Ecosystems: Preliminary Evaluation." *Eleventh Forest Service Remote Sensing Applications Conference*. 2006.
- Burgess, M. A., et al. "A Small Unmanned Aircraft System for Ecological Research." *AUVSI's Unmanned Systems North America*. Poster, 2009.
- Burgess, M. A., P. G. Ifju, H. F. Percival, J. H. Perry, and S. E. Smith. "Development of a survey-grade sUAS for natural resource assessment and monitoring." *Florida Cooperative Fish and Wildlife Research Unit Annual Coordinating Committee Meeting*. Gainesville, FL: Slide presentation, May 23, 2009.
- Deperrois, A. *XFLR5 v6.03 [Software]*. 2011. <http://xflr5.sourceforge.net/xflr5.htm>.
- Drela, M. *Mark Drela Tail Airfoils*. July 2001.  
[http://www.charlesriverrc.org/articles/drelaairfoils/markdrela\\_tailairfoils.htm](http://www.charlesriverrc.org/articles/drelaairfoils/markdrela_tailairfoils.htm)  
(accessed October 2011).
- . *Quick V-Tail Sizing*. March 2000.  
[http://www.charlesriverrc.org/articles/design/markdrela\\_vtailsizing.htm](http://www.charlesriverrc.org/articles/design/markdrela_vtailsizing.htm) (accessed October 2011).

- . *SuperGee I Pod Molding*. October 2003. [http://www.charlesriverrc.org/articles/supergee/pod\\_molding.pdf](http://www.charlesriverrc.org/articles/supergee/pod_molding.pdf) (accessed October 2011).
- Durand, W. F. "Tests on Thirteen Navy Type Model Propellers." *NACA Technical Report 237*, 1927.
- Federal Aviation Administration. *Glider Flying Handbook*. Skyhorse Publishing, 2007.
- Hepperle, M. *Drag of Linkages*. August 2003. <http://www.mh-aerotoools.de/airfoils/linkage.htm> (accessed October 2011).
- Hepperle, M. "Neue Profile für Elektro-Pylonmodelle." *FMT-Kolleg 10*, 1991.
- Jensen, J. *Introductory Digital Image Processing*. Prentice Hall, 2004.
- Jones, G. P. "The Feasibility of Using Small Unmanned Aerial Vehicles for Wildlife Research." *Master's Thesis*. University of Florida, 2003.
- Lee, K. H. "Development of Unmanned Aerial Vehicle (UAV) for Wildlife Surveillance." *Master's Thesis*. University of Florida, 2004.
- MacArthur, D., J. K. Schueller, and C. D. Crane. "Remotely-Piloted Mini-Helicopter Imaging of Citrus." *American Society of Agricultural and Biological Engineers*, 2005.
- Magnuson, S. "Military Swimming in Sensors and Drowning in Data." *National Defense*, January 2010.
- Nyquist, J. "Applications of Low-Cost Radio-Controlled Airplanes to Environmental Restoration at Oak Ridge National Laboratory." 1996.
- Owen, P. "When the Ravens Met the Sandhill Cranes." *Unmanned Systems*, June 2011.
- Perry, J. H. "A Synthesized Directly Georeferenced Remote Sensing Technique for Small Unmanned Aerial Vehicles." *Master's Thesis*. University of Florida, 2009.
- Perry, J. H., Evers, B. S., Rambo, T. J., Reed, T. M., Burgess, M. "Natural Resource Management with a Small Unmanned Aircraft." *AUVSI's Unmanned Systems North America*. 2011.
- Phillips, W. F. *Mechanics of Flight*. John Wiley & Sons, 2004.
- Pisanich, G., and S. Morris. "Fielding an Amphibious UAV: Development, Results, and Lessons Learned." *Digital Avionics Systems Conference*. 2002.

- Rubio, J., and S. Kragelund. "The Trans-Pacific Crossing: Long Range Adaptive Path Planning for UAVs through Variable Wind Fields." *Digital Avionics Systems Conference*. 2003.
- Santamaria, E., P. Royo, C. Barrado, E. Pastor, J Lopez, and X. Prats. "Mission Aware Flight Planning for Unmanned Aerial Systems." *AIAA Guidance, Navigation and Control Conference*, 2008.
- Selig, M. S., C. Lyon, P. Giguere, C. Ninham, and J. Guglielmo. *Summary of Low-Speed Airfoil Data, Volume 2*. SoarTech, 1996.
- Selig, M. S., Donovan, J., and Fraser, D. *Airfoils at Low Speeds*. Soartech, 1989.
- Vorse, B. "Unmanned Aerial Vehicle Taking Fight on Invasive Species to New Heights." *JaxStrong*, February 2011.
- Wilkinson, B. E. "The Design of Georeferencing Techniques for Unmanned Autonomous Aerial Vehicle Video for Use with Wildlife Inventory Surveys: A Case Study of the National Bison Range, Montana." *Master's Thesis*. University of Florida, 2007.
- Wolf, P. R., and B. A. Dewitt. *Elements of Photogrammetry with Applications in GIS*. McGraw-Hill, 2000.

## BIOGRAPHICAL SKETCH

Brandon Scott Evers was born and grew up in Lake Wales, FL. From an early age, his passion for flight and all things mechanical led him towards a career in aviation. Upon graduation from the International Baccalaureate School in Bartow, FL, Brandon attended the University of Florida on a National Merit Scholarship. Pursuing a degree in Aerospace Engineering, he eventually joined UF's Micro Air Vehicles Lab, where his practical engineering education began. Contributing to projects ranging from an air-dropped bomb damage assessment MAV to an entry in the US-European MAV Competition, he developed valuable experience in rapid design and composite manufacturing techniques while working under Dr. Peter Ifju. Brandon obtained his B.S. in Aerospace Engineering in 2009 and immediately began his graduate studies at the University of Florida. He continued to work on UAV-related projects, designing the Nova 2.1 sUAS in collaboration with fellow UF UASRG researchers. In addition to his roles in system design and fabrication, Brandon also served as the remote pilot for field deployments of the Nova 2.1 and was responsible for training and certification of external system operators from the USACE.

With FAA sUAS restrictions providing additional incentive to pursue a lifelong goal, Brandon obtained his Private Pilot Glider rating in 2011, introducing him to the world of silent flight, which provided some of the inspiration for his thesis work. During his graduate studies, Brandon also rediscovered a love for the outdoors, and enjoys spending more time than is practical mountain biking, backpacking, and kayaking with his incredibly willing fiancée throughout North Florida.